Supporting Information: Triplet dynamics reveal loss pathways in multi-resonance thermally activated delayed fluorescence emitters

Alexandra N. Stuart,[*,†,‡] Katrina Bergmann,[¶] Inseong Cho,[†,‡] William J. Kendrick,[§,‡] Zachary M. Hudson,[¶] Wallace W. H. Wong,[§,‡] and Girish Lakhwani[*,†,‡]

†*Department of Chemistry, The University of Sydney, Camperdown, New South Wales, 2000, Australia*
‡*Australian Research Council Centre of Excellence in Exciton Science, Parkville 3010, Australia*
¶*Department of Chemistry, The University of British Columbia, Vancouver, British Columbia, Canada, V6T 1Z1*
§*School of Chemistry, The University of Melbourne, Parkville 3010 VIC, Australia*

E-mail: a.stuart@sydney.edu.au; girish.lakhwani@sydney.edu.au

Contents

Supporting information

S1   Experimental methods

OQAO(mes)$_2$ was synthesized as reported previously.[1] Solutions were prepared with toluene, chloroform, chlorobenzene, and *o*-dichlorobenzene (all anhydrous >99%, Merck) in sealed cuvettes in a glovebox under a nitrogen atmosphere. The oxygen content of the glovebox was kept below 10 ppm. For oxygen experiments air was bubbled through cuvettes containing the solution prepared under N$_2$ for approximately 5 min.

Steady-state absorption spectra were collected using a Cary-60 (Agilent) UV-visible spectrophotometer. Steady-state emission spectra were recorded using a RF-6000 (Schimadzu) fluorimeter, exciting at 450 nm. Photoluminescence quantum yields were recorded using a Edinburgh Instruments FS5 fluorimeter with an integrating sphere.

Time-resolved emission data were collected using a time-correlated single photon counting (TCSPC) setup (Deltaflex, HORIBA). Prompt emission decays were collected in TCSPC mode, using 450 nm excitation pulse generated from a white-light continuum pulsed laser at a repetition rate of 1.22 MHz (NKT SuperK Extreme), and a monochromator. Delayed emission was measured using the same set up in multichannel scaling (MCS) mode, with 450 nm excitation generated from a white-light continuum pulsed at 1326 Hz (NKT Compact), passed through a 450 nm bandpass filter. Excitation fluences for all emission experiments were below 5 µW.

Transient absorption spectra were collected on a commercial nanosecond-timescale transient absorption spectrophotometer (EOS, Ultrafast Systems). The excitation pulse was 355 nm pulse at a 700 Hz repetition rate, with a full-width at half maximum (FWHM) spot size of 0.5 mm at the sample. The probe pulse was generated from a photonic crystal fiber based supercontinuum laser (EOS, Ultrafast systems), split into signal and referenced beams, with a 0.1 mm FWHM spot size at the sample. The polarization of the excitation pulse was rotated to magic angle relative to the probe pulse. The excitation fluence was 0.9 mW (650 µJ) unless otherwise noted.

S2   Time-resolved emission data

Individual traces for each solvent under N_2 and after exposure to air (labeled O_2) are shown for prompt emission in Figure S1 and delayed emission in Figure S2. The delayed emission is significantly accelerated under air, indicating the quenching of the triplet state(s). This is likely via interactions with ground state oxygen causing the sensitization of singlet oxygen:

$$T_n + {}^3O_2 \rightarrow S_0 + {}^1O_2.$$
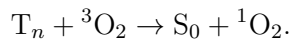
The prompt emission background becomes much lower after exposure to air, due to the decrease in delayed emission, but the prompt decay is also slightly accelerated, indicating the interaction of $OQAO(mes)_2$ singlet excitons with oxygen. This could occur via the process

$$S_1 + {}^3O_2 \rightarrow T_n + {}^1O_2,$$
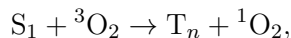
but since the energy gap of S_1 and T_n should be much smaller than the energy needed to excite singlet oxygen (0.97 eV), this is unlikely. It is more likely that singlets are reacting with existing singlet oxygen (e.g. generated from the $OQAO(mes)_2$ triplets) via

$$S_1 + {}^1O_2 \rightarrow T_n + {}^3O_2.$$
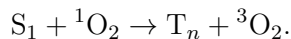
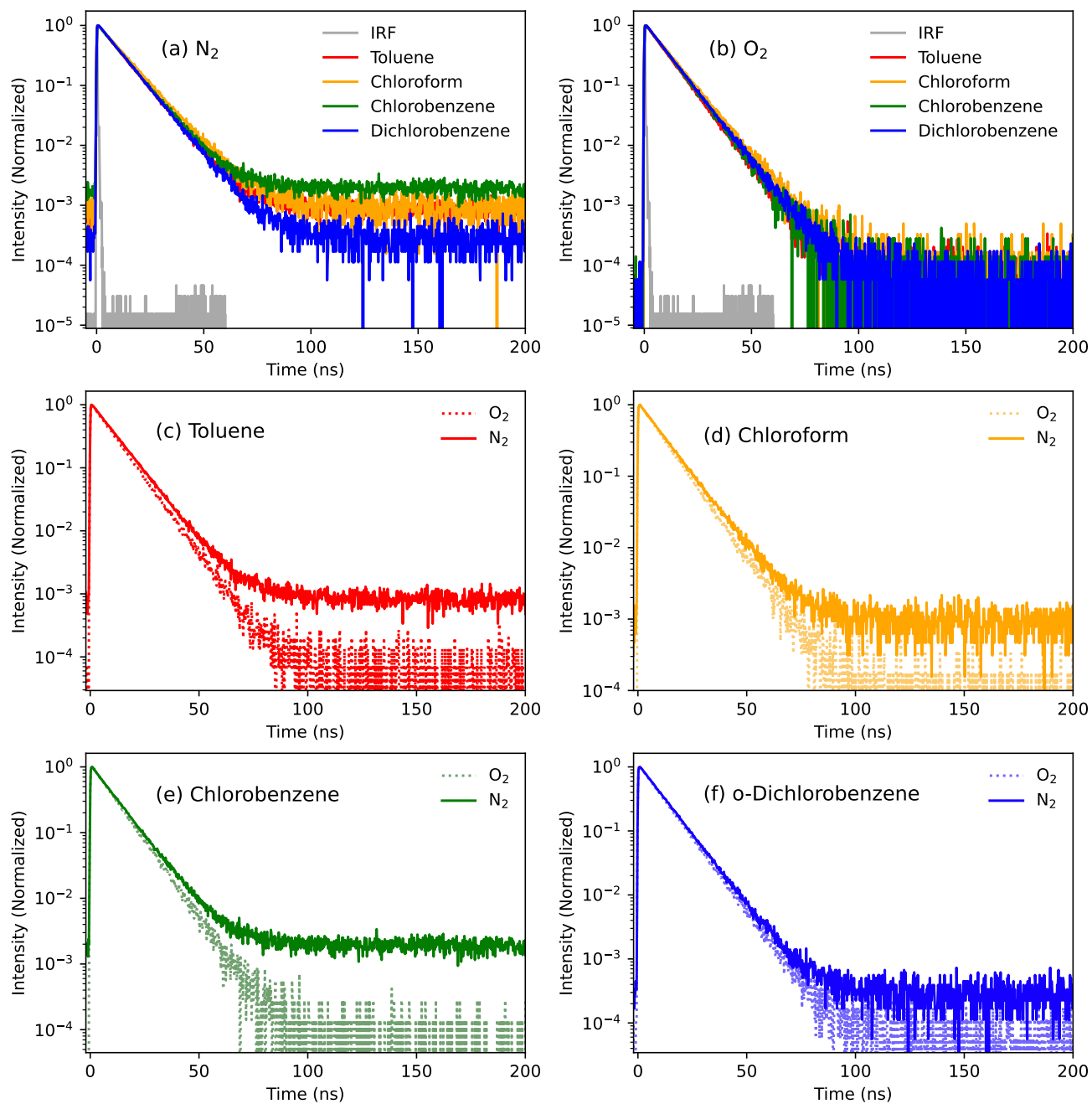These types of interactions have previously been observed to occur in organic materials.[2,3]

Figure S1: Prompt emission (showing singlet exciton lifetimes) from time correlated single photon counting (TCSPC) data for OQAO(mes)$_2$ in different solvents. TCSPC was measured after solutions were prepared and sealed in cuvettes a glovebox (N$_2$) and then after bubbling air through the same cuvettes (O$_2$).

Figure S2: Delayed emission from multichannel scaling (MCS) data for OQAO(mes)$_2$ in different solvents. TCSPC was measured after solutions were prepared and sealed in cuvettes a glovebox (N$_2$) and then after bubbling air through the same cuvettes (O$_2$).
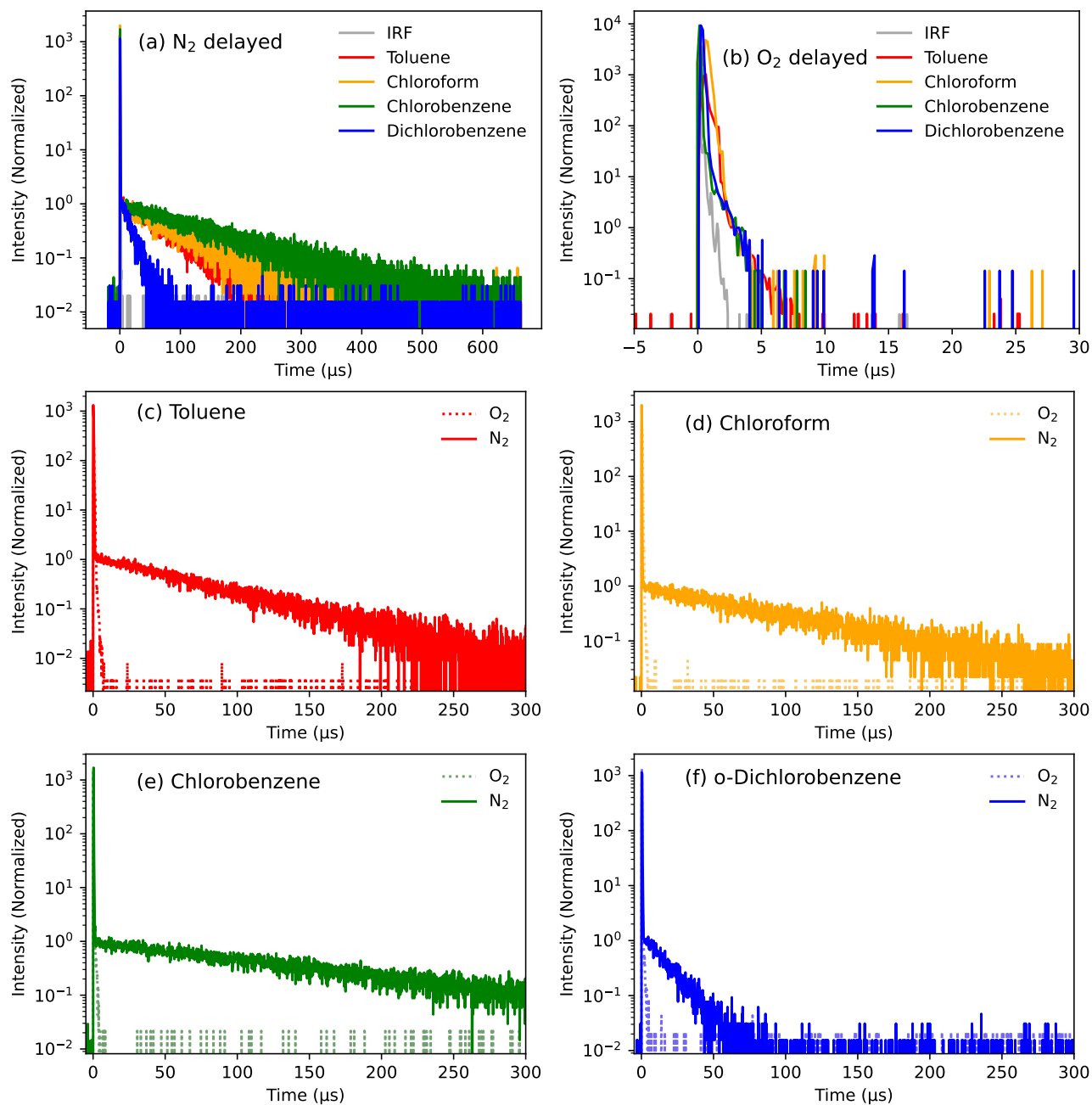
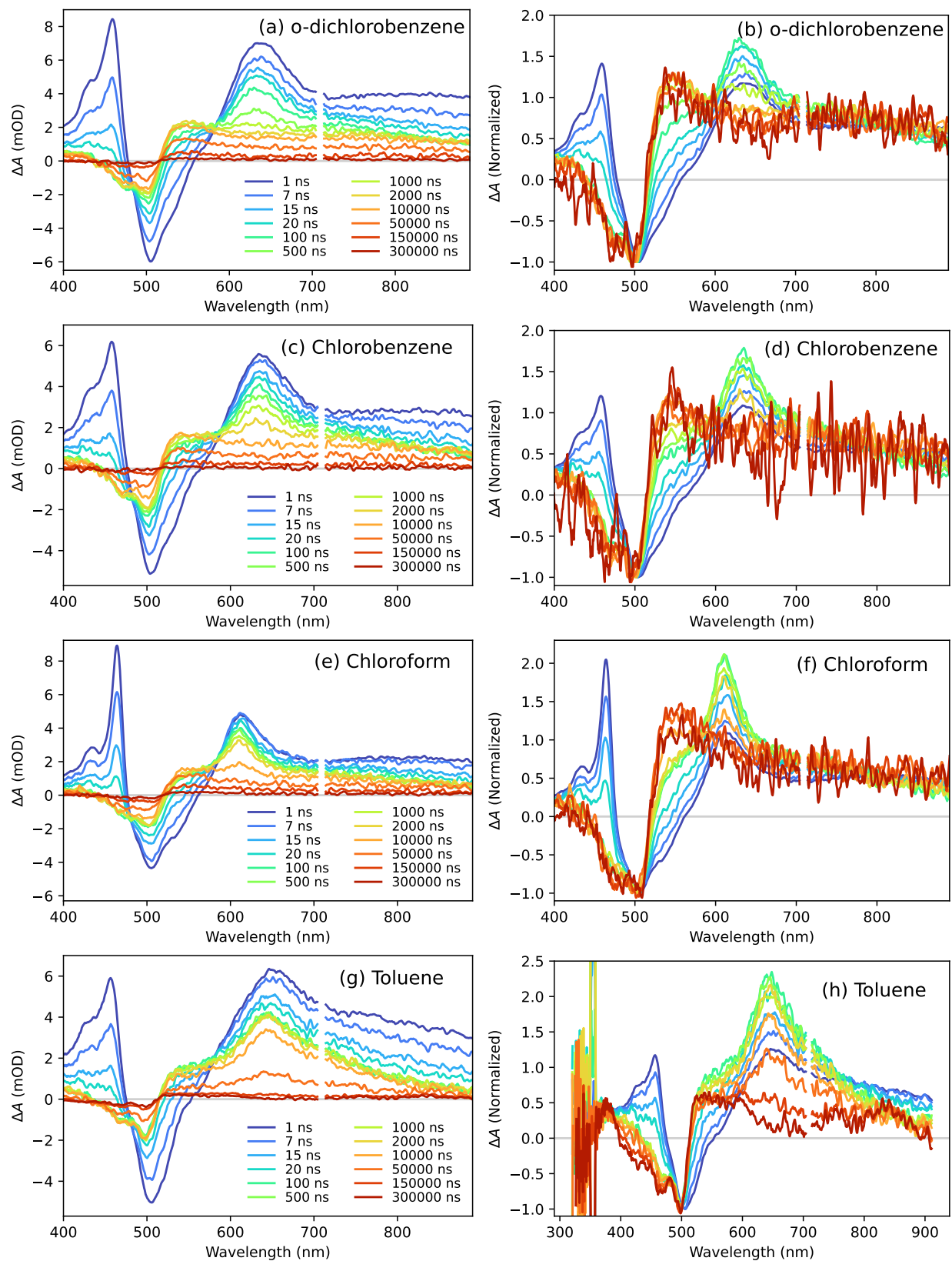# S3   Transient absorption data

Figure S3: TA spectra of OQAO(mes)$_2$ in various solvents under N$_2$ at 298 K, excited at 355 nm. (a), (c), (e) and (g) show the raw TA spectra, and (b), (d), (f) and (h) show the TA spectra normalized to the ground state bleach (GSB). Data is omitted from 705–715 nm due to scattering of the excitation pulse. All solutions were excited at 355 nm at 0.9 mW.

S4   TA Deconvolution

S4.1   2-component deconvolution

We initially attempt to deconvolute the TA spectrum of OQAO(mes)$_2$ in *o*-dichlorobenzene with just two components, which we arbitrarily label A and B. The basis spectrum of component A, $\epsilon_A(\lambda)$, is taken from the TA spectrum at early times (1 ns), and the basis spectrum of B, $\epsilon_B(\lambda)$, is taken from late times (500 µs). Then the TA spectrum can be fit as a linear combination of the component A and component B basis spectrum at each time, t, using

$$\Delta A(\lambda, t) = \epsilon_A(\lambda)c_A(t) + \epsilon_B(\lambda)c_B(t), \tag{S1}$$

where $c_A(t)$ and $c_B(t)$ are the concentrations of component A and B at time t, respectively. The basis spectra ($\epsilon_A(\lambda)$ and $\epsilon_B(\lambda)$) are shown in Figure S4a, and the resulting concentrations of A and B in Figure S4b. The fit of the 2-component deconvolution (i.e. the fit of Equation 1) to the data is shown in Figures S5 and Figures S6, where it can be seem the fits are poor, particularly at intermediate times (2 ns<t<10000 ns). It is clear the TA data cannot be reproduced with only 2 components, and a third spectral component is needed.

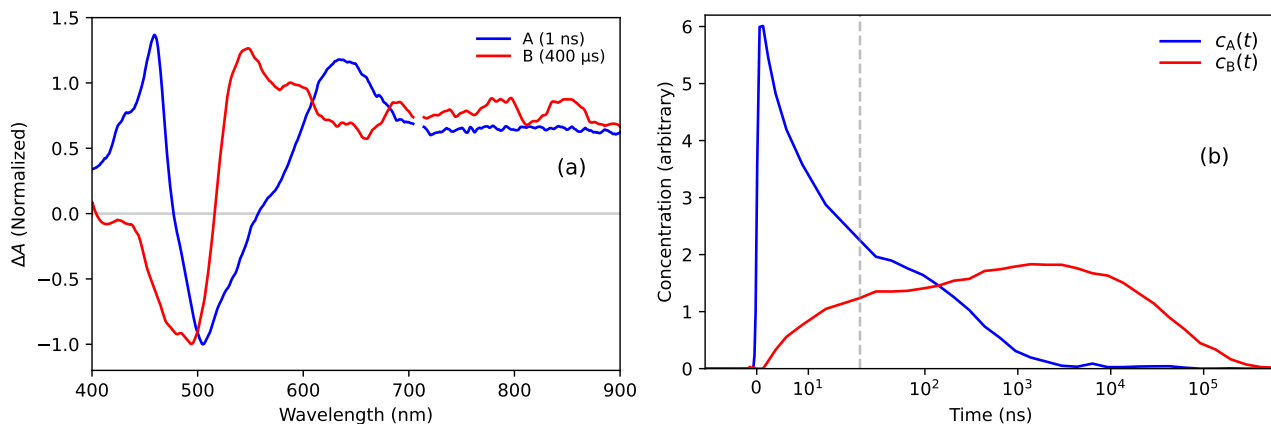**Figure S4:** (a) Basis spectra for the 2-component deconvolution of OQAO(mes)$_2$ in *o*-dichlorobenzene. Both spectra are normalized to the GSB. The spectrum of component B (taken at 500 µs) has been smoothed with a Savitzky-Golay filter. (b) Concentration of component A and B from the 2-component deconvolution of OQAO(mes)$_2$ in *o*-dichlorobenzene. The vertical dashed line indicates a change from linear to log scale.
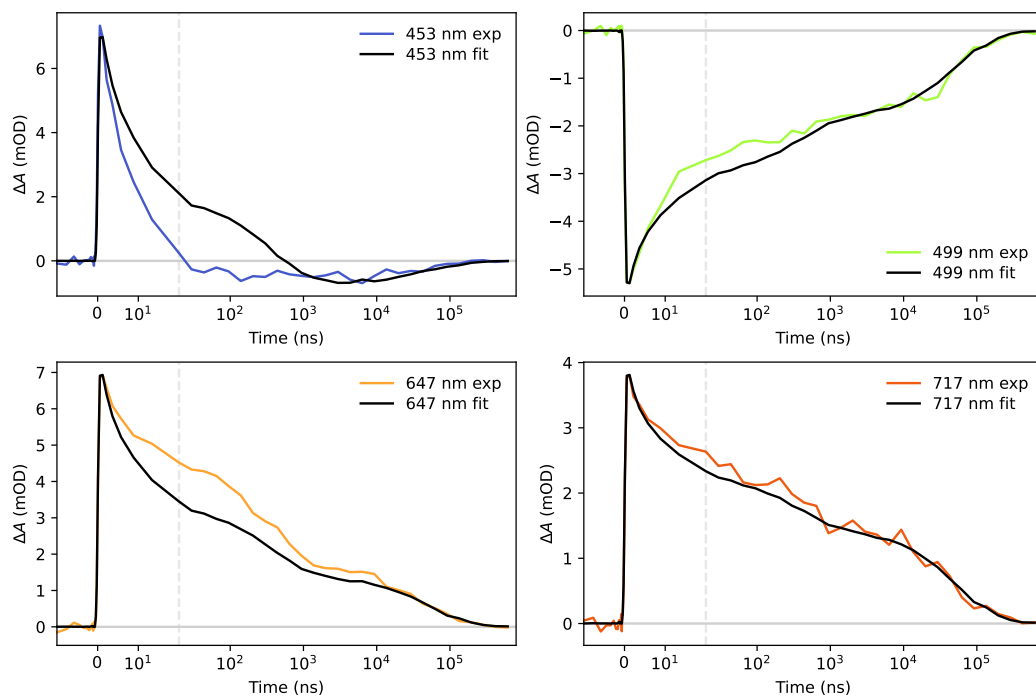
Figure S5: Fit of the 2-component deconvolution to the TA data of OQAO(mes)$_2$ in *o*-dichlorobenzene at selected wavelengths. The vertical dashed line indicates a change from linear to log scale on the time axis.
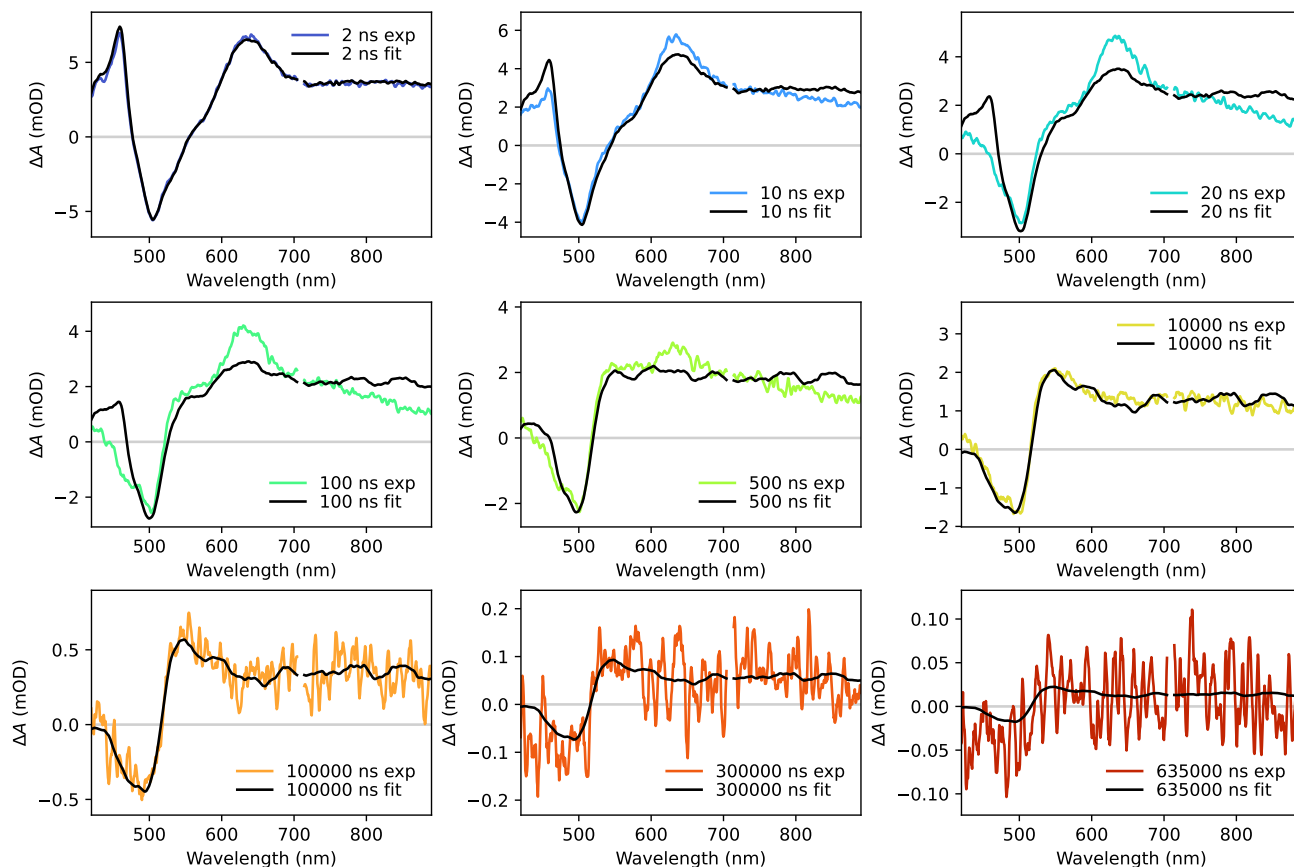

Figure S6: Fit of the 2-component deconvolution to the TA data of OQAO(mes)$_2$ in *o*-dichlorobenzene at selected times.

S4.2   3-component deconvolution

To reproduce the TA data we extract three spectral components, initially labeled A, B, and C, such that the spectra can be described by

$$\Delta A(\lambda, t) = \epsilon_A(\lambda)c_A(t) + \epsilon_B(\lambda)c_B(t) + \epsilon_C(\lambda)c_C(t). \tag{S2}$$

The basis spectrum of A is again taken from the TA spectra from very early times (1 ns) to avoid contamination from component B and C as they form. Likewise, the basis spectrum of C is taken at very late times ($>500\,\mu s$) to avoid contamination of A and B. The spectral shape of the TA spectrum is relatively constant after $\sim100\,\mu s$, so we assume that only one component is present after that time (C). However determining the basis spectrum of the intermediate component, B, is less straightforward. We use 55 ns to extract component B, since this is the maximum of the peak at 630 nm (relative to the GSB) that was unable to be captured by the 2-component fit. However it is very possible that the spectrum at 55 ns is not due to a single component. The features of component A (i.e. the ESA at 460 nm and SE at $\sim540\,$nm) have mostly gone by 50 ns, so we can assume that A has negligible contribution. But it is possible that component C is also present at 50 ns. We thus consider two extreme scenarios:

1. There is no component C contribution at 55 ns, and the entirety of the spectrum is due to component B:

$$\Delta A(\lambda, 55 \text{ ns}) = \epsilon_B(\lambda)c_B(55 \text{ ns}) \tag{S3}$$

$$\therefore \epsilon_B(\lambda) = \frac{\Delta A(\lambda, 55 \text{ ns})}{c_B(55 \text{ ns})}. \tag{S4}$$

   We refer to this as the upper bound for B.

2. There is significant C contribution at 55 ns, and the spectrum is due to the sum of both B and C. In other words:

$$\Delta A(\lambda, 55 \text{ ns}) = \epsilon_B(\lambda)c_B(55 \text{ ns}) + \epsilon_C(\lambda)c_C(55 \text{ ns}) \tag{S5}$$

$$\therefore \epsilon_B(\lambda) = \frac{\Delta A(\lambda, 55 \text{ ns}) - \epsilon_C(\lambda)c_C(55 \text{ ns})}{c_B(55 \text{ ns})}, \tag{S6}$$

   where the minimum amount of $c_C(55 \text{ ns})$ is 0 (i.e. scenario 1, upper bound for B). The maximum amount of $c_C(55 \text{ ns})$ can be determined from the shape of the spectrum. It is unfeasible for component B to have negative ΔA signal outside of the GSB and SE (~450–$550\,$nm), however if too much component C is subtracted a negative signal around 750 nm appears. Hence the maximum amount of $c_C(50 \text{ ns})$ is the highest concentration before $\epsilon_B(750 \text{ nm})$ becomes negative. This gives us the lower bound for B.

We can therefore deconvolute the TA data using these possibilities as upper and lower limits for the B component basis spectrum. The resulting basis spectra are shown in Figure S7 for o-dichlorobenzene, where the upper and lower bounds of B are the lower and upper limits of the black shaded area. Note that the actual concentrations or extinction coefficients are unknown, so the basis spectra are normalized to the ground state bleach. As a result, the concentrations resulting from the fit have arbitrary units. The fit of the 3-component deconvolution to the data is shown in Figures S9 and Figure S8, where it can be seen that the spectra are reproduced well at all wavelengths and times. We conclude that three spectral components are thus sufficient to reproduce the data.

The three component deconvolution was repeated for OQAO(mes)$_2$ in chlorobenzene, chloroform, and toluene, as shown in Figure S10–S18. In all cases, three components are able to reproduce the data well.
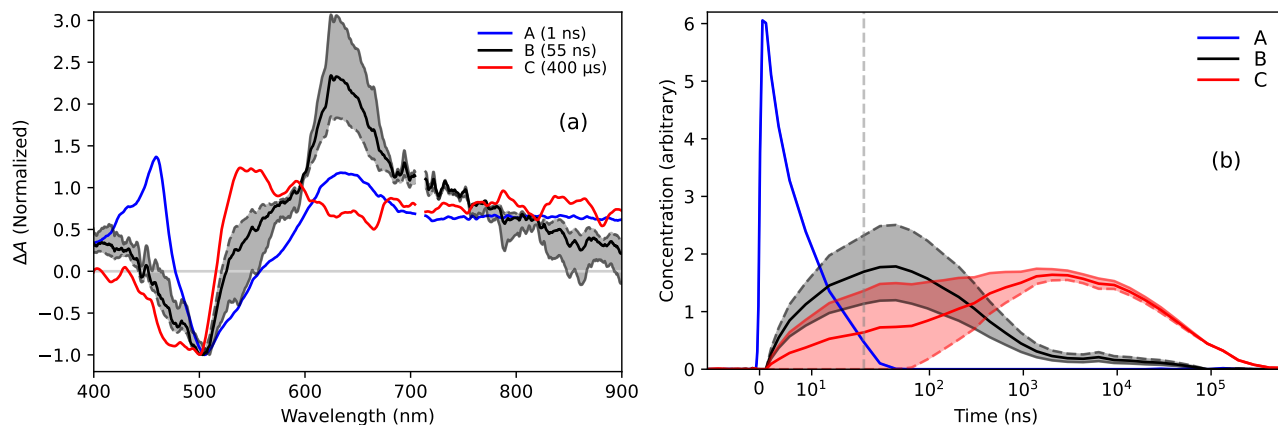
Figure S7: (a) Basis spectra for 3-component deconvolution of OQAO(mes)$_2$ in o-dichlorobenzene. Spectra are normalized to the GSB. The spectrum of component C (taken at 400 µs) has been smoothed with a Savitzky-Golay filter. Data are omitted at 710 nm due to scatter from the excitation pulse. (b) Concentrations of components A, B, and C from the 3-component deconvolution of OQAO(mes)$_2$ in o-dichlorobenzene. The basis spectra and concentrations determined from the upper bound (assuming no component C at 55 ns) are shown in gray/light-red dashed lines, and the lower bound in gray/light-red solid lines. A mid-bound is also shown in solid black/red as a guide to the eye.

Figure S8: Fit of the 3-component deconvolution to the TA data of OQAO(mes)$_2$ in o-dichlorobenzene at selected wavelengths. The vertical dashed line indicates a change from linear to log scale on the time axis.

Figure S9: Fit of the 3-component deconvolution to the TA data of OQAO(mes)$_2$ in *o*-dichlorobenzene at selected times.

Figure S10: (a) Basis spectra for 3-component deconvolution of OQAO(mes)$_2$ in chlorobenzene. Spectra are normalized to the GSB. The spectrum of component C (taken at 400 µs) has been smoothed with a Savitzky-Golay filter. Data are omitted at 710 nm due to scatter from the excitation pulse. (b) Concentrations of components A, B, and C from the 3-component deconvolution of OQAO(mes)$_2$ in chlorobenzene. The basis spectra and concentrations determined from the upper bound (assuming no component C at 55 ns) are shown in gray/light-red dashed lines, and the lower bound in gray/light-red solid lines. A mid-bound is also shown in solid black/red as a guide to the eye.
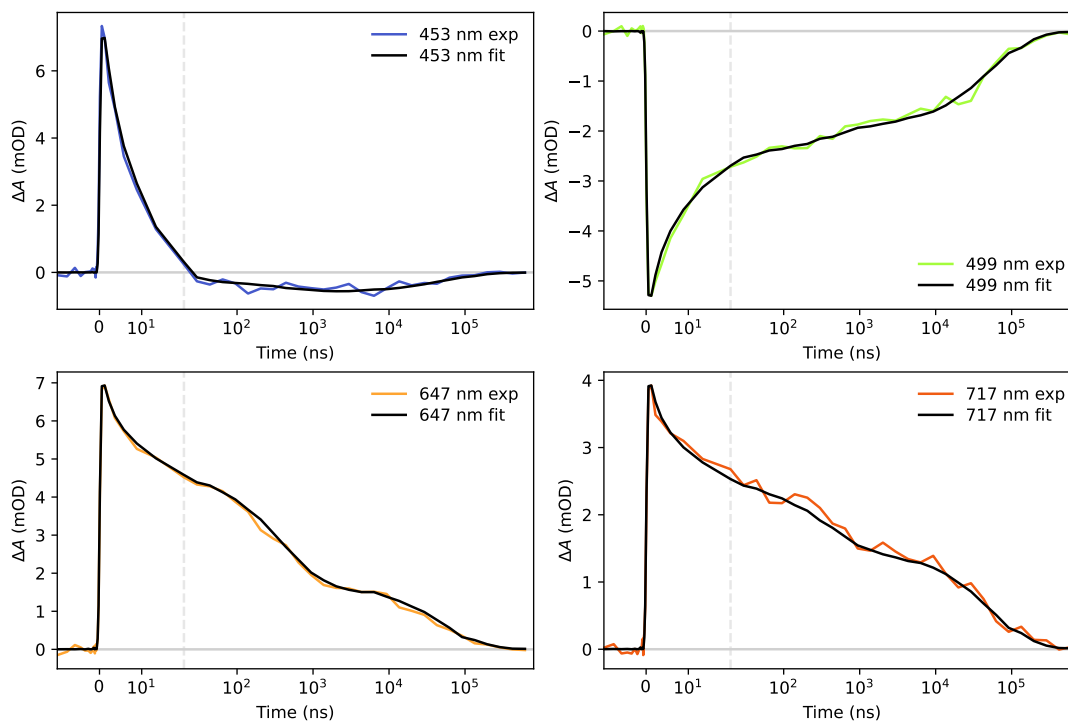
Figure S11: Fit of the 3-component deconvolution to the TA data of OQAO(mes)$_2$ in chlorobenzene at selected wavelengths. The vertical dashed line indicates a change from linear to log scale on the time axis.
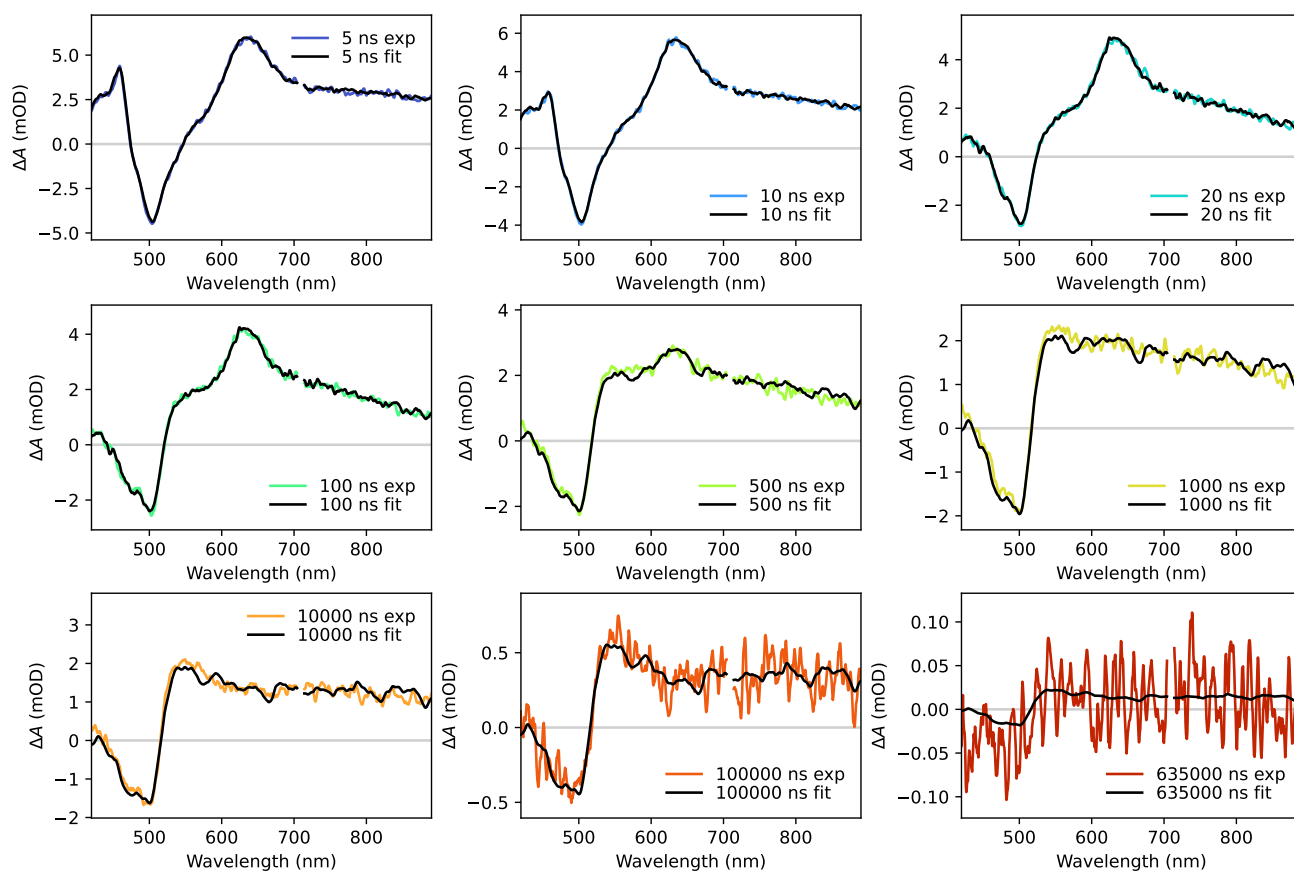

Figure S12: Fit of the 3-component deconvolution to the TA data of OQAO(mes)$_2$ in chlorobenzene at selected times.
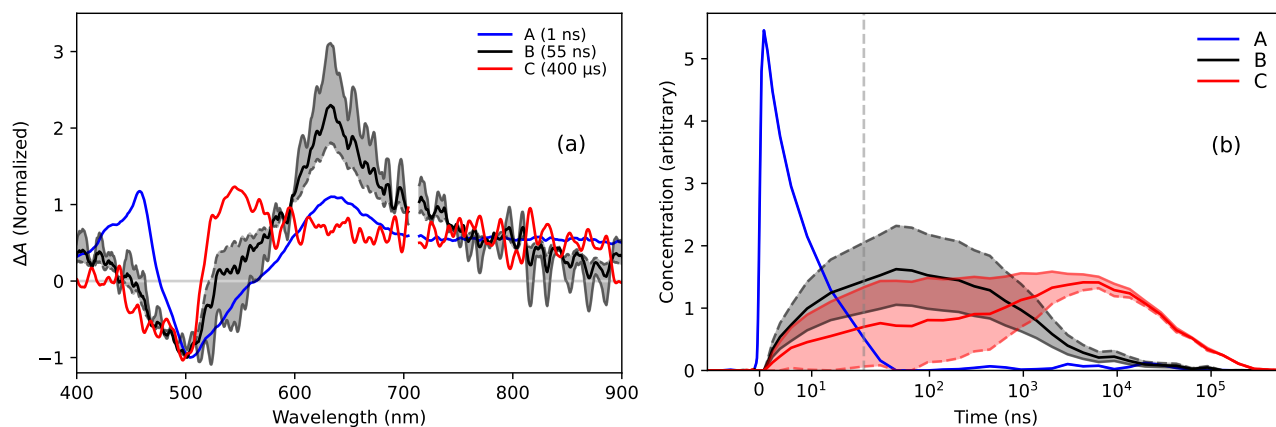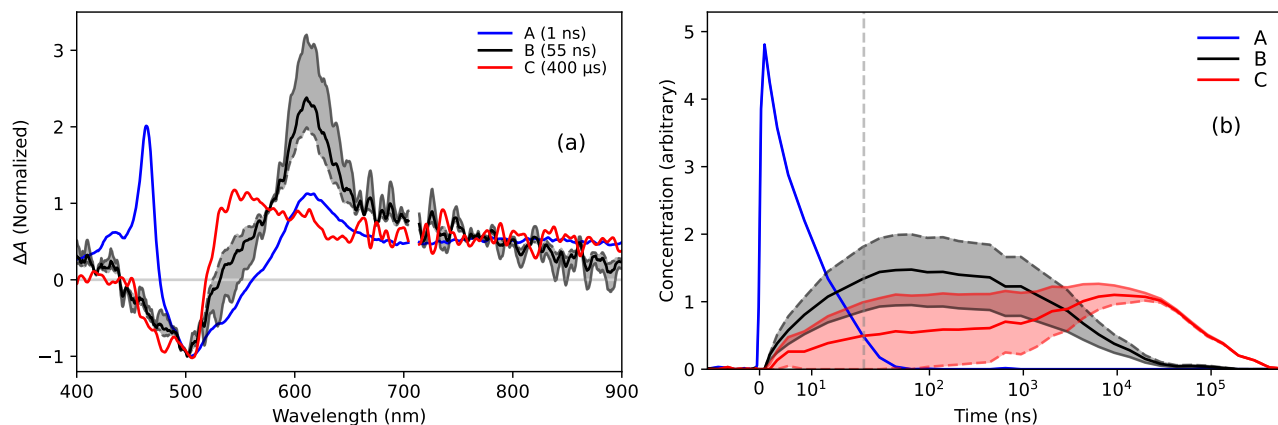
Figure S13: (a) Basis spectra for 3-component deconvolution of OQAO(mes)$_2$ in chloroform. Spectra are normalized to the GSB. The spectrum of component C (taken at 400 μs) has been smoothed with a Savitzky-Golay filter. Data are omitted at 710 nm due to scatter from the excitation pulse. (b) Concentrations of components A, B, and C from the 3-component deconvolution of OQAO(mes)$_2$ in chloroform. The basis spectra and concentrations determined from the upper bound (assuming no component C at 55 ns) are shown in gray/light-red dashed lines, and the lower bound in gray/light-red solid lines. A mid-bound is also shown in solid black/red as a guide to the eye.
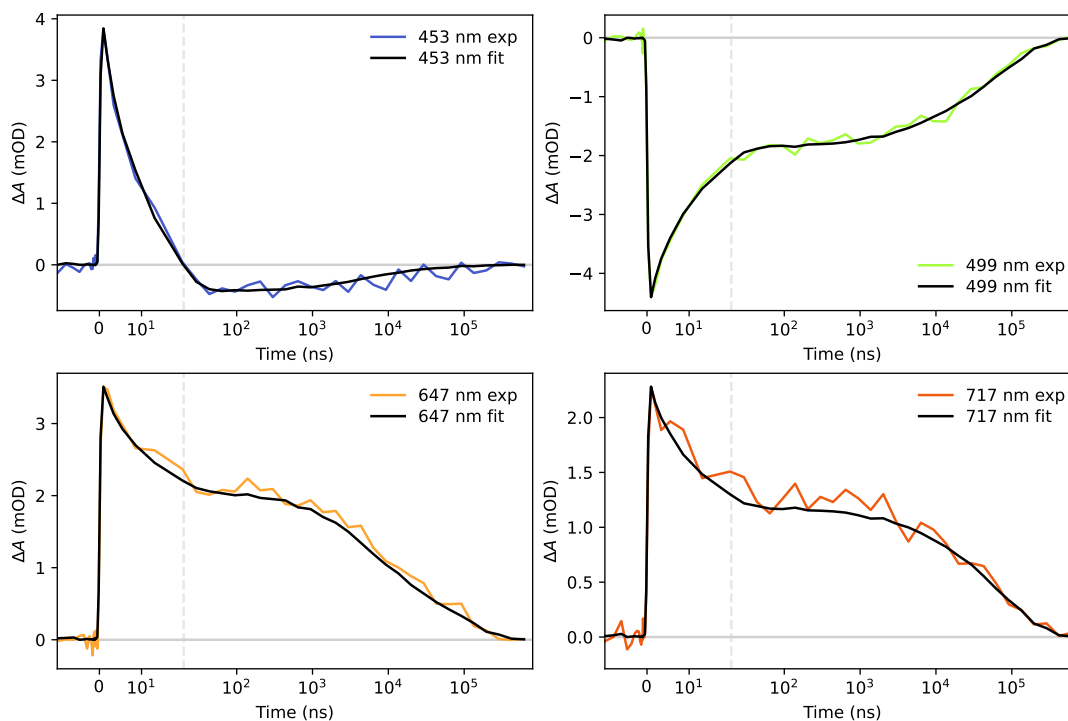
Figure S14: Fit of the 3-component deconvolution to the TA data of OQAO(mes)$_2$ in chloroform at selected wavelengths. The vertical dashed line indicates a change from linear to log scale on the time axis.
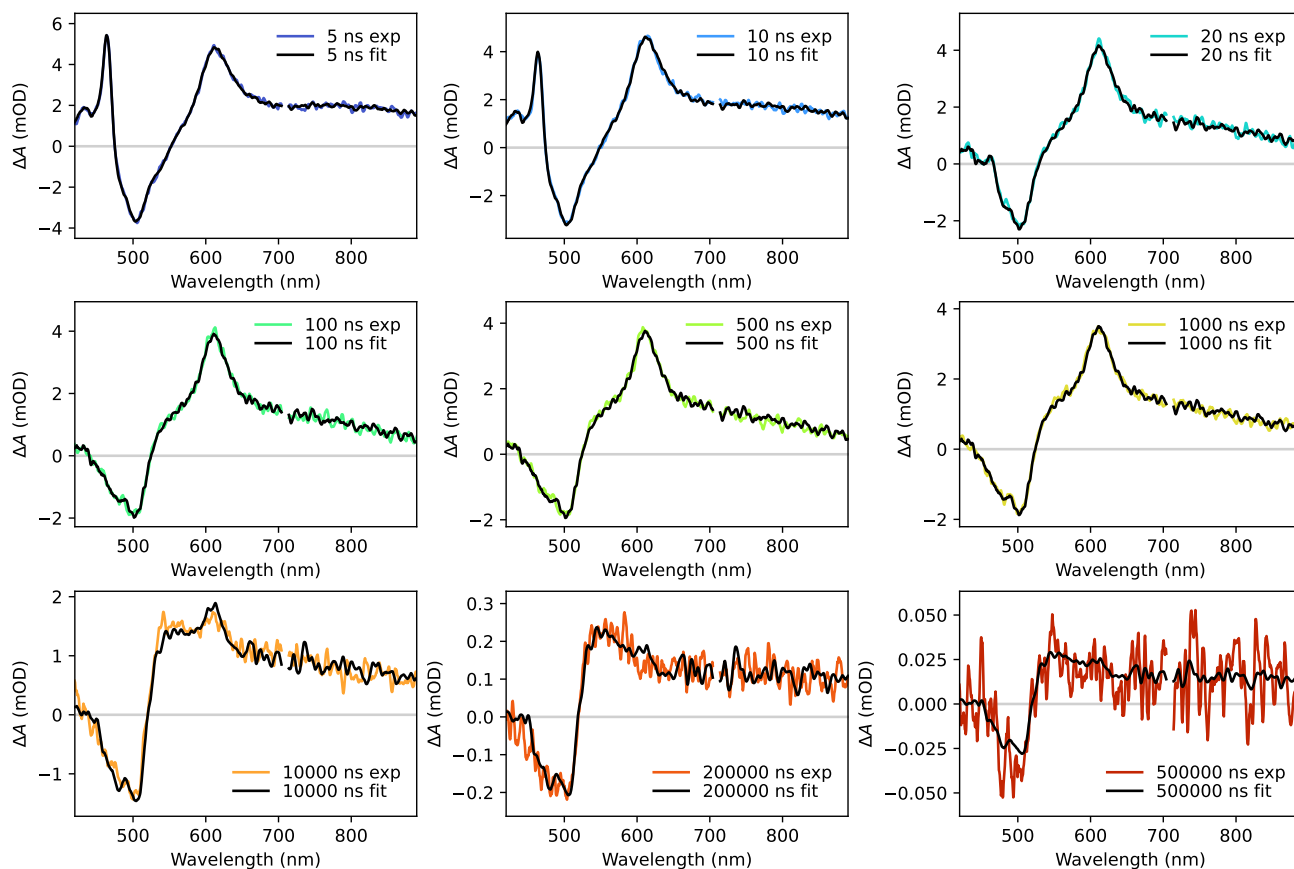
Figure S15: Fit of the 3-component deconvolution to the TA data of OQAO(mes)$_2$ in chloroform at selected times.
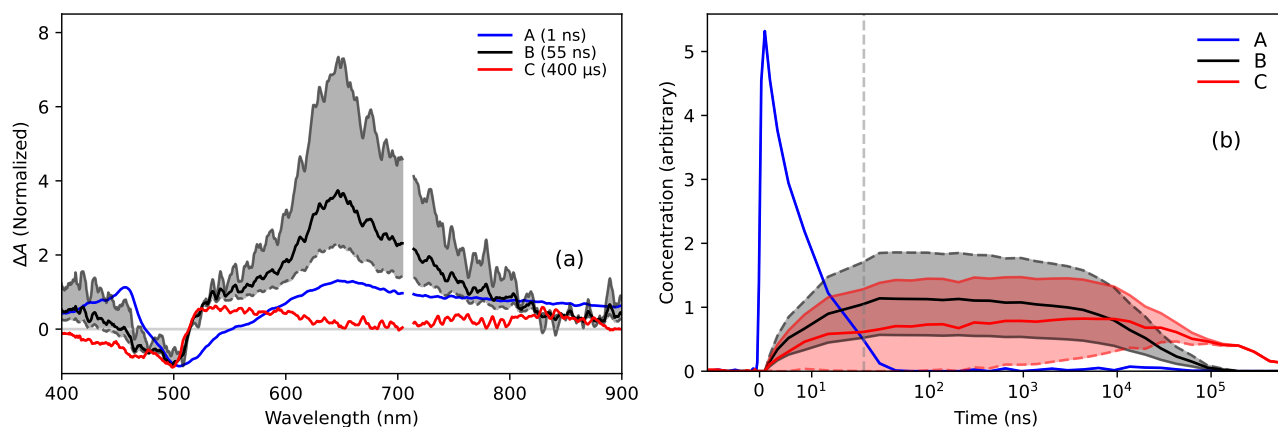
Figure S16: (a) Basis spectra for 3-component deconvolution of OQAO(mes)$_2$ in toluene. Spectra are normalized to the GSB. Data are omitted at 710 nm due to scatter from the excitation pulse. (b) Concentrations of components A, B, and C from the 3-component deconvolution of OQAO(mes)$_2$ in toluene. The basis spectra and concentrations determined from the upper bound (assuming no component C at 55 ns) are shown in gray/light-red dashed lines, and the lower bound in gray/light-red solid lines. A mid-bound is also shown in solid black/red as a guide to the eye.
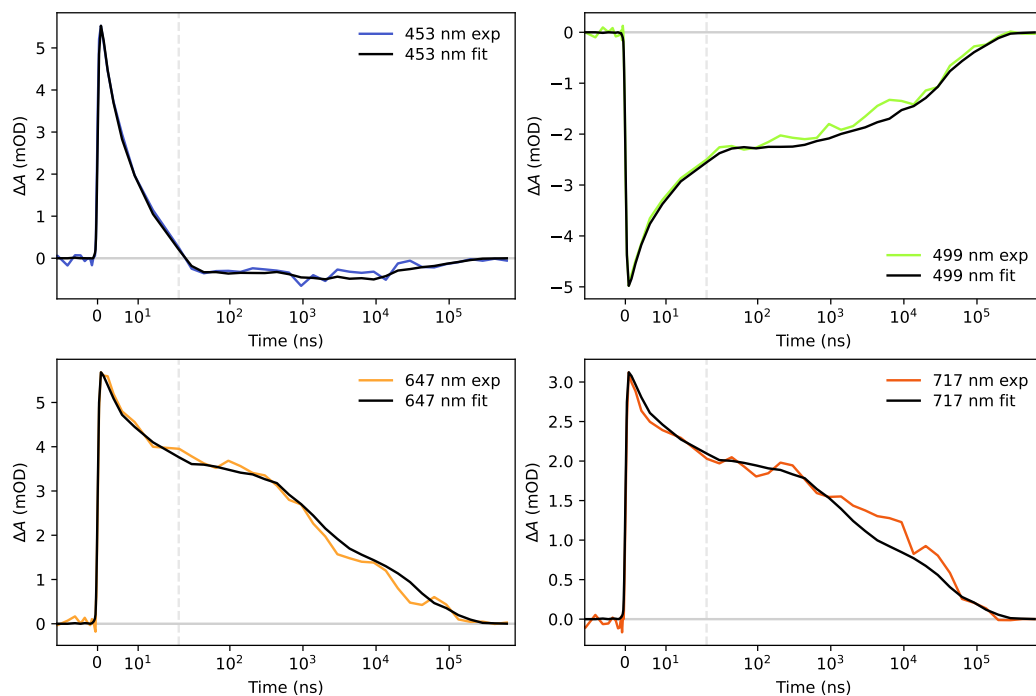
Figure S17: Fit of the 3-component deconvolution to the TA data of OQAO(mes)$_2$ in toluene at selected wavelengths. The vertical dashed line indicates a change from linear to log scale on the time axis.
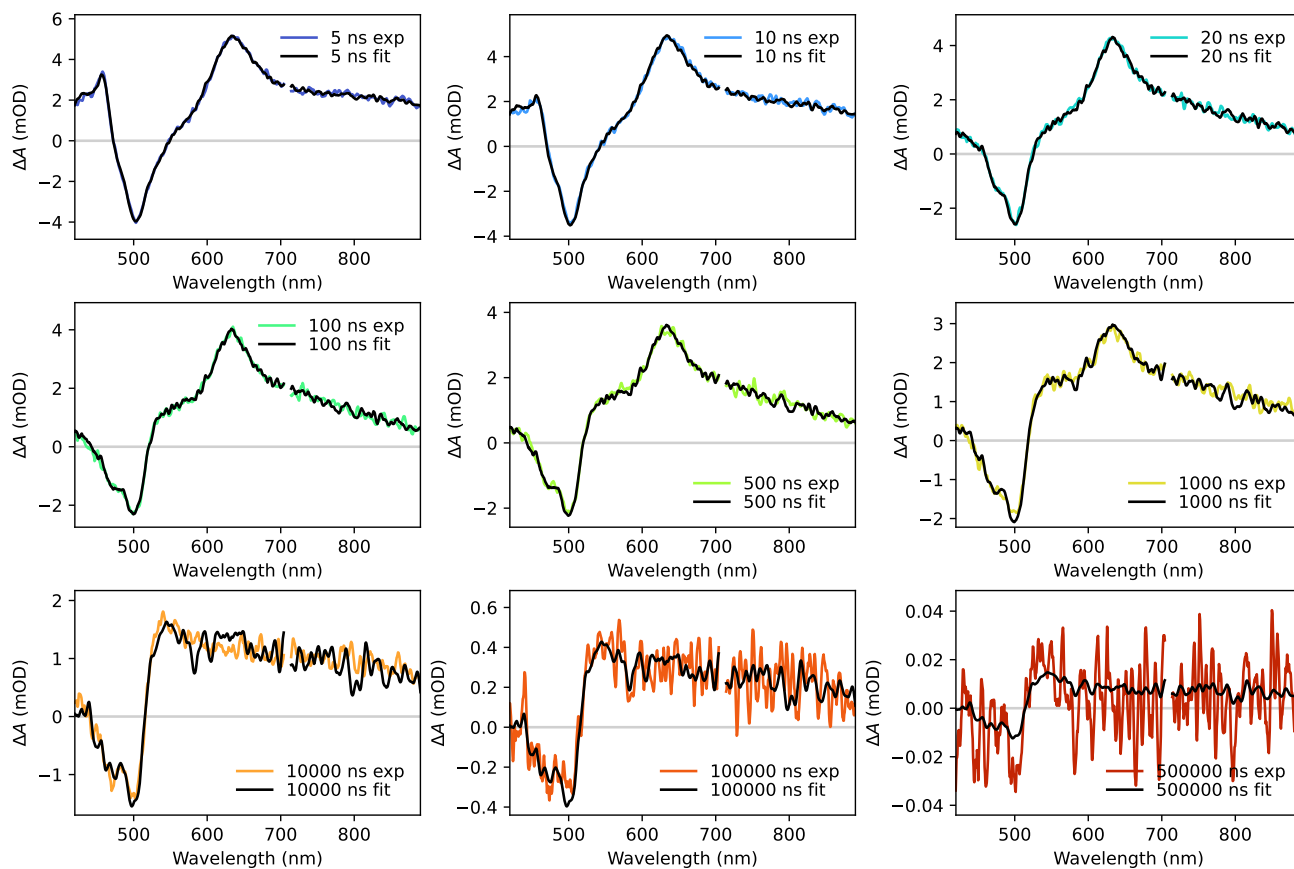

Figure S18: Fit of the 3-component deconvolution to the TA data of OQAO(mes)$_2$ in toluene at selected times.
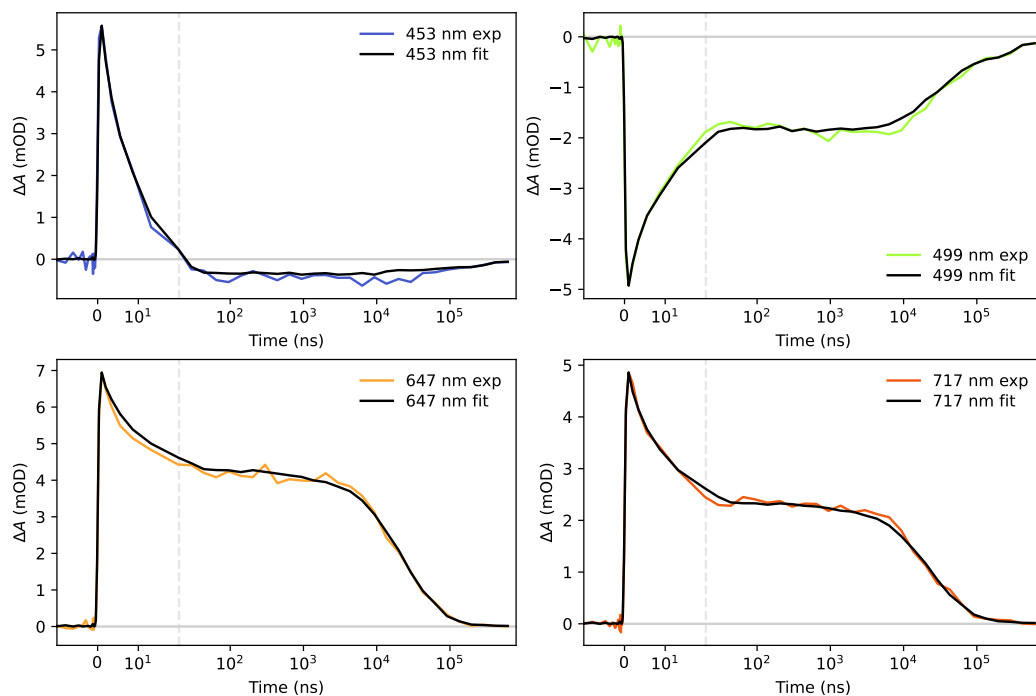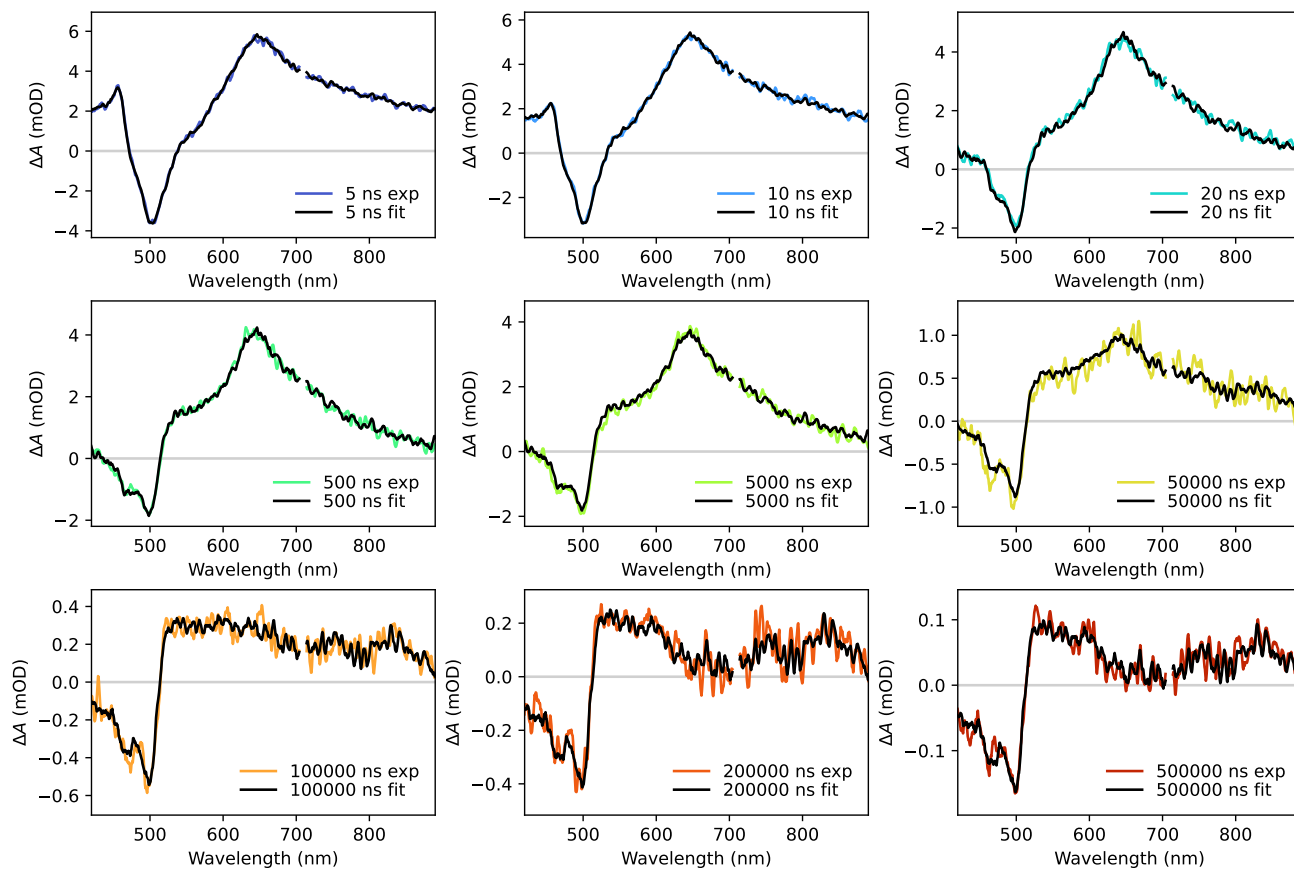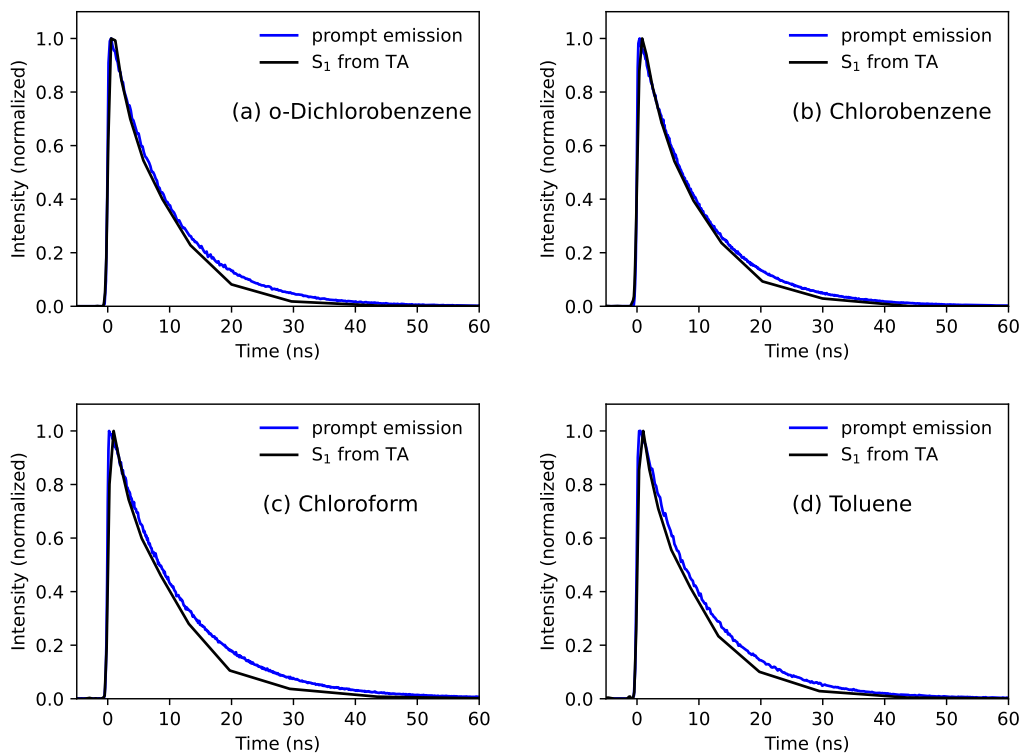
S4.3   Spectral assignment

Figure S19: Deconvoluted concentration of component A (from TA data) and prompt emission decay from time correlated single photon counting (TCSPC) measurements.

Figure S19 shows the decay of species A from TA deconvolution and the prompt emission measured using TCSPC decay for OQAO(mes)$_2$ in each solvent, which match closely in all cases. This agreement and the observation of stimulated emission features in the component A basis spectra leads us to confidently assign component A as the singlet excited state, S$_1$. Some TADF studies refer to the singlet excited state as ^{1}CT, however since the CT character in OQAO(mes)$_2$ is weak, we refrain from this.

Since components B and C exist on nano–microsecond timescales and are not strongly emissive, we assign these as triplet states. This is confirmed by triplet sensitization experiment with 4CzIPN as discussed in Section S5. We refer to component B as the early-time triplet, T$_{early}$, and C as the late-time triplet, T$_{late}$. The two extremes for the basis spectrum of B lead to very different kinetics for the rise of C. Using *o*-dichlorobenzene as an example (Figure S7b), for the upper limit basis spectrum, component C is formed very slowly, and the rise is correlated with the decay of component B. Thus would suggest a sequential model of the form A $\longrightarrow$ B $\longrightarrow$ C, where A $\longrightarrow$ B is very fast (10s of ns), while B $\longrightarrow$ C is very slow (1000s of ns). The lower limit basis spectrum results in components B and C rising concurrently, with B decaying on a faster timescale than C. This is more reminiscent of a model of the form A $\longrightarrow$ B + C $\longrightarrow$ C, i.e. both B and C are formed from A, with B decaying on a faster timescale. However, we note from Figure S7b that component C continues to rise long after minimal A is present, and the rise on this timescale correlates with the decay of B regardless of the basis spectrum used, suggesting some B $\longrightarrow$ C must occur. In other words, some T$_{early}$ $\longrightarrow$ T$_{late}$ must occur, presumably via internal conversion, regardless of which basis spectrum used.

As discussed in the main text, TDDFT calculations allow the calculation of spin-orbit coupling (SOC) constants between the singlet and triplet states of OQAO(mes)$_2$. Additionally, SOC calculations indicate that ISC to the higher energy triplet state, T$_2$ is possible, but the SOC constant between S$_1$ and T$_1$ is

low, so ISC to this state is unlikely. Hence, we propose that component B/T_{early} in the main text is T_2, and component C/T_{late} is T_1. Thus B $\longrightarrow$ C is internal conversion from $T_2 \longrightarrow T_1$. We therefore consider A $\longrightarrow$ C, i.e. $S_1 \longrightarrow T_1$, to be unlikely, ruling out the kinetics determined from the lower limit basis spectrum. Finally, we also show in Section S8.3 below that the lower bound kinetics are unable to be reproduced by a kinetic model as well as the upper bound kinetics, further suggesting the sequential evolution is more likely. In the main text, we only show kinetics determined from the upper limit basis spectrum.

Note that as the choice of basis spectrum only affects the rise time of T_{late}, it does not alter the agreement (or lack of) of the triplet kinetics with the delayed emission, as demonstrated in Figure S20. In other words, regardless of T_{early} basis spectrum used, the T_{early} decay closely matches the delayed emission decay for toluene and chlorobenzene, and agreement of chloroform and *o*-dichlorobenzene remain ambiguous (as discussed in the main text).
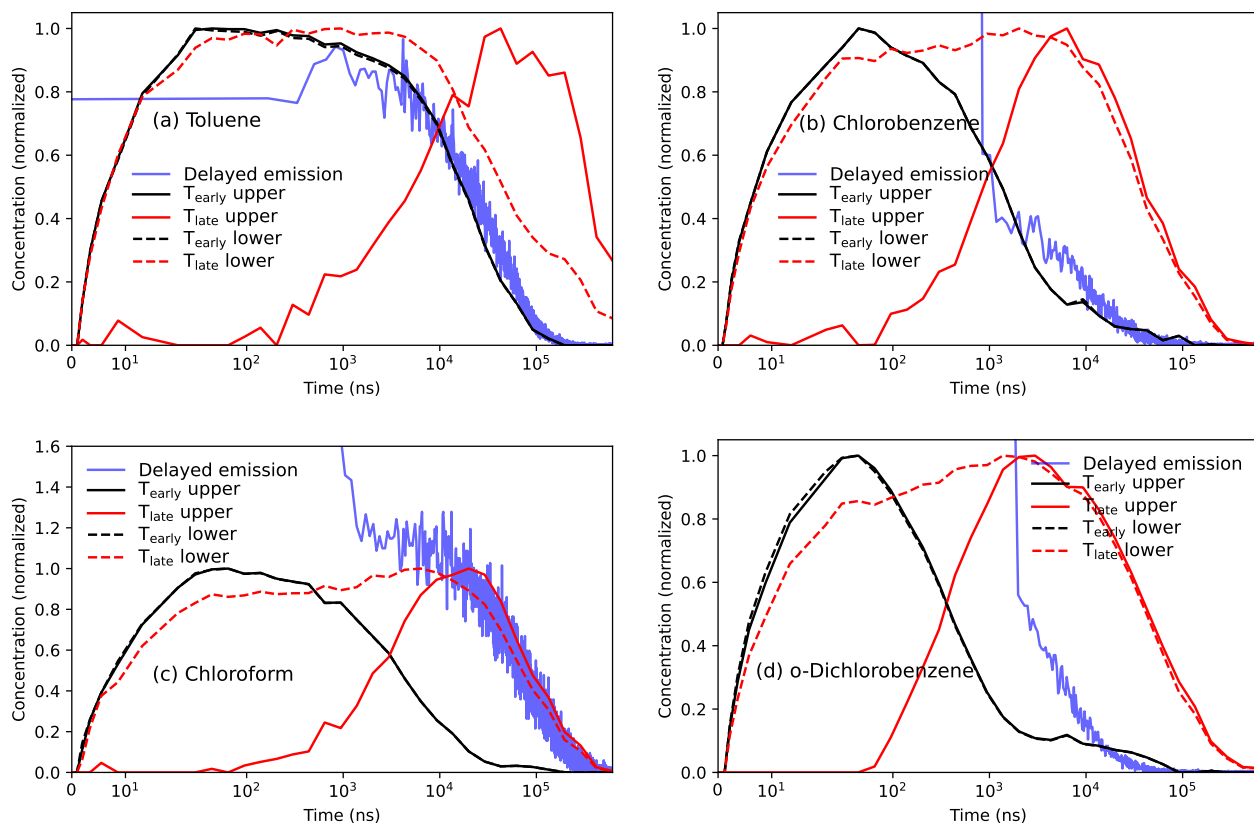
Figure S20: Deconvoluted concentrations of T_{early} and T_{late} from the TA data of OQAO(mes)$_2$ in various solvents using both upper and lower bounds of the T_{early} basis spectra, plot with the delayed emission data. Delayed emission is scaled to best match either T_{early} or T_{late}.

S5   Triplet sensitization

The donor-acceptor TADF molecule 4CzIPN has a triplet energy of 2.53 eV (as measured from phosphorescence in toluene at 77K).[4] Based on the singlet-triplet energy gap of OQAO(mes)$_2$ determined previously,[1] we expect a triplet energy around 2.2 eV in toluene. Hence 4CzIPN should be able to sensitize triplets excitons in OQAO(mes)$_2$, allowing us to identify the OQAO(mes)$_2$ triplet absorption spectrum in TA. The steady-state absorption of a blend solution of approximately 18 µM 4CzIPn and 67 µM

OQAO(mes)$_2$ in toluene is shown in Figure S21, alongside the spectra of neat 4CzIPN and OQAO(mes)$_2$ toluene solutions.
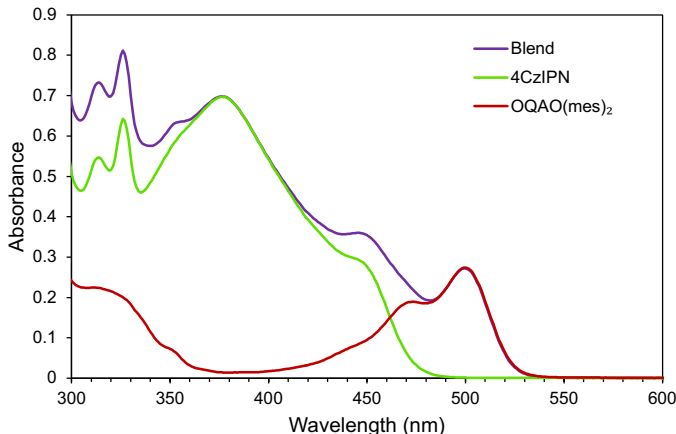
Figure S21: Steady-state absorption spectra of the 4CzIPN/OQAO(mes)$_2$ blend used for triplet sensitization. Also shown are the spectra of neat 4CzIPN and neat OQAO(mes)$_2$, scaled to their relative contribution to the blend spectra. Toluene is the solvent used in all cases.

We first determined the TA basis spectra of the 4CzIPN singlet and triplet excitons. TA was collected of a neat solution of 4CzIPN in toluene under N$_2$, exciting at 355 nm. The resulting spectrum is shown in Figure S22a. We deconvoluted this spectrum into two components using the data at 1 and 50 ns (Figure S22b), and fit the data to a linear combination of these components, as described above for OQAO(mes)$_2$. The resultant fits are shown in Figures S23 and S24. The spectra fit well at all times, indicating that only two components are required to fit the 4CzIPN TA spectra, which is consistent with previous TA studies on this material.[5,6] The 4CzIPN has significant charge transfer character, so the early time component can be described as a singlet CT state, ^{1}CT. Two triplet states are involved in 4CzIPN TADF, a local exciton triplet (^{3}LE) and a CT triplet (^{3}CT). According to previous studies, these triplets exist in equilibrium and so the triplet state observed in TA likely corresponds to both.[5,6]

The TA spectrum of the 4CzIPN/OQAO(mes)$_2$ blend in toluene under N$_2$ is shown in Figure S25. 4CzIPN absorbs significantly more at the excitation wavelength of 355 nm, so the early time spectra should be dominated by 4CzIPN excitons, however some OQAO(mes)$_2$ will be excited as well. Correspondingly, at early times the features are dominated by 4CzIPN, but at later times OQAO(mes)$_2$ features corresponding to components B and C determined above become evident. To determine the relative proportions of each excited state present, the TA was fit using the neat 4CzIPN basis spectra in Figure S22b and neat OQAO(mes)$_2$ basis spectra in Figure S16b (only the upper bound basis spectra were used for OQAO(mes)$_2$). The basis spectra from the two neat solutions are able to reproduce the blend TA well at all times, as shown in Figures S26 and S27.

The deconvoluted concentrations of each component in the blend TA are shown in Figure S28. A comparison of the singlet and triplet kinetics of 4CzIPN in neat toluene TA and in the blend TA is shown in Figure S28b. The 4CzIPn triplets decay faster in the blend than in the neat, suggesting an additional triplet quenching pathway, such as triplet energy transfer. A comparison of the singlet and triplet kinetics of OQAO(mes)$_2$ in neat toluene TA and in the blend TA is shown Figure S28c. At early times, the kinetics are identical to the neat OQAO(mes)$_2$ case, however after about 100 ns the T$_{early}$ component begins to grow significantly larger in the blend solution. Figure S28a shows that this growth in T$_{early}$ occurs on the same timescale that 4CzIPN T$_1$ decays, indicating that there is triplet energy transfer from 4CzIPN to OQAO(mes)$_2$. This confirms that component B (T$_{early}$) observed in the OQAO(mes)$_2$ spectrum is indeed a triplet state, and that it has an energy below that of the 4CzIPN triplet (2.53 eV). Component C (T$_{late}$) is also much larger in the blend than neat case, consistent with

the sensitized T_{early} states continuing to evolve to T_{late}.

Note that the amount of sensitized triplet in OQAO(mes)$_2$ looks disproportionally large in Figure S28c compared to the relatively small change in triplet decay for 4CzIPN in Figure S28b. However, when we consider than the concentration of initially excited OQAO(mes)$_2$ excitons is much smaller than 4CzIPN this is reasonable- a small amount of 4CzIPN triplets can sensitize a large proportion of OQAO(mes)$_2$ triplets. Singlet energy transfer from 4CzIPN to OQAO(mes)$_2$ is also theoretically possible, but in this case appears to be outcompeted by ISC and radiative decay.
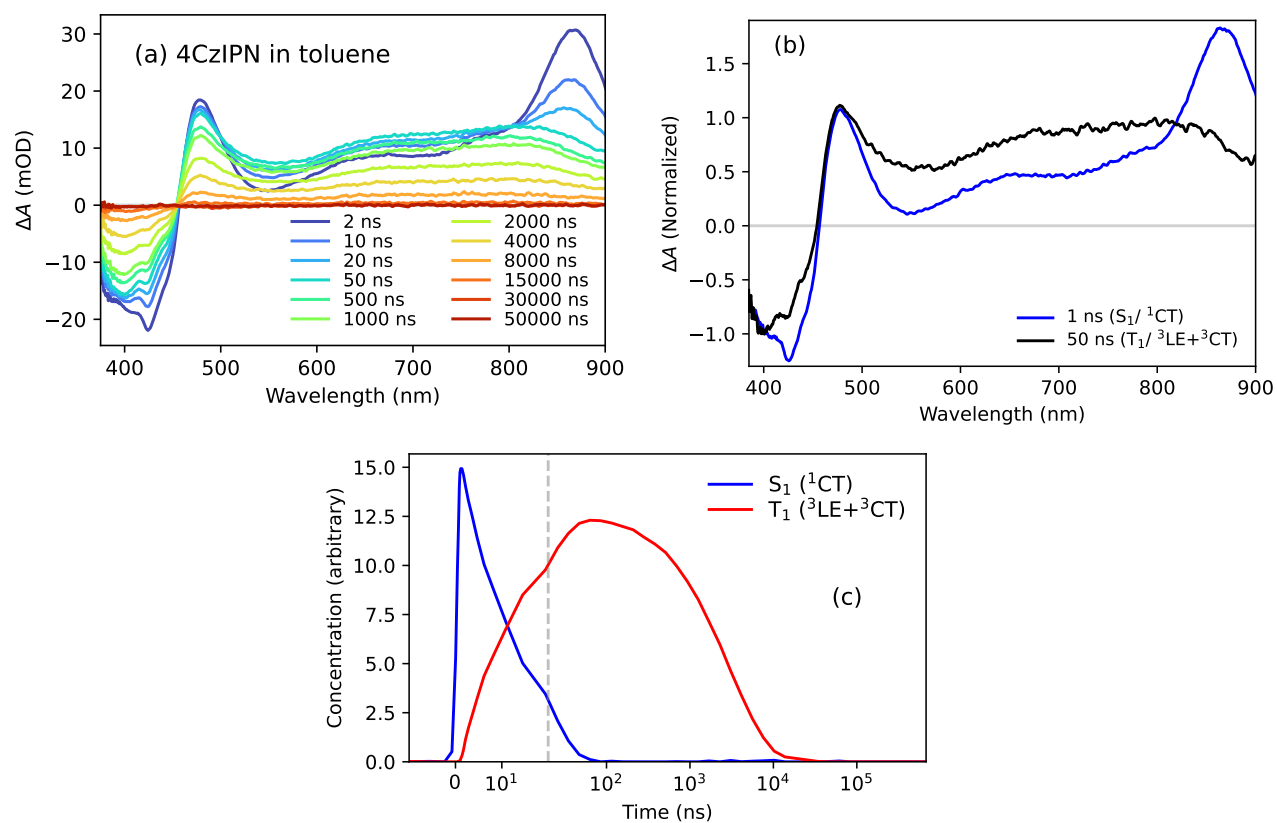
Figure S22: (a) TA spectrum of 4CzIPN in toluene under N_2, excited at 355 nm. (b) Singlet and triplet basis spectra of 4CzIPN in toluene, normalized to 400 nm, and (c) deconvoluted singlet and triplet concentrations using the basis spectra in (b). Note the S_1 and T_1 concentrations are not necessarily to scale.
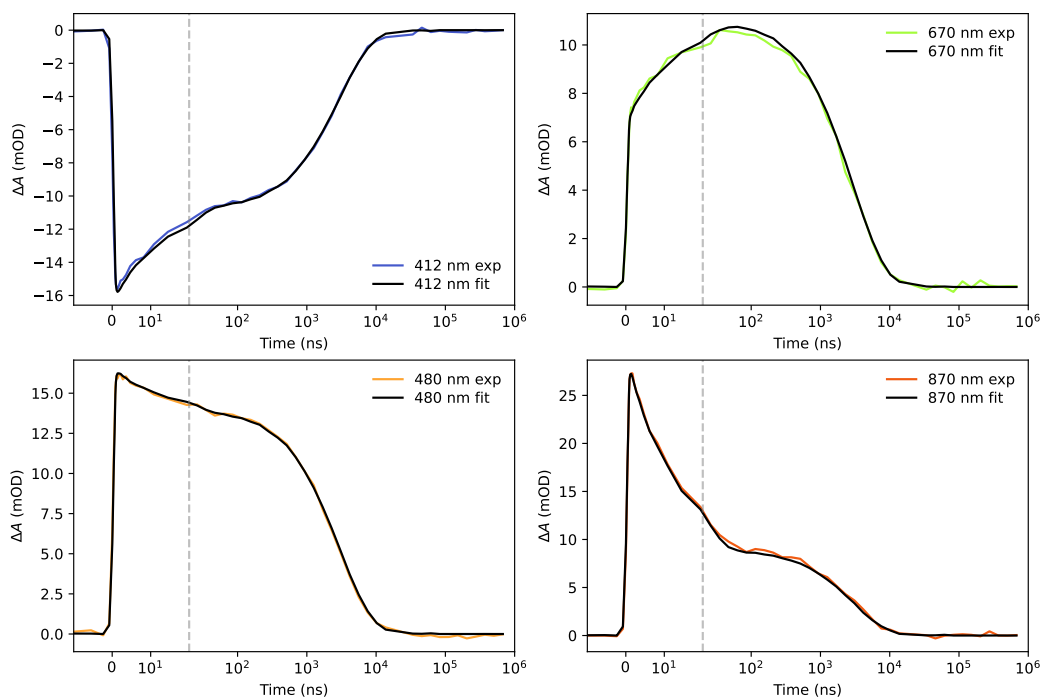
Figure S23: Fit of the 2-component deconvolution to the TA data of 4CzIPN in toluene at selected wavelengths. The vertical dashed line indicates a change from linear to log scale on the time axis.
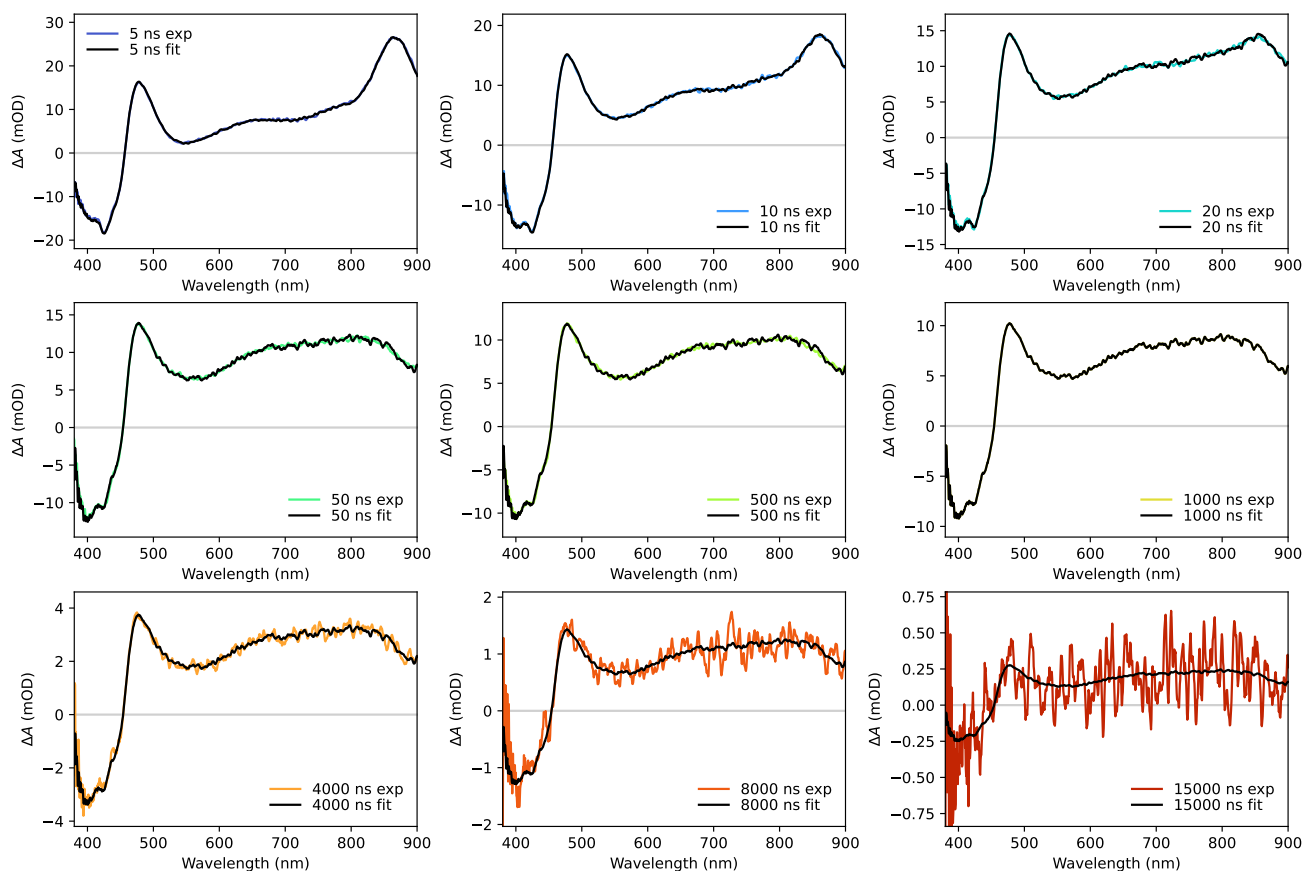
Figure S24: Fit of the 2-component deconvolution to the TA data of 4CzIPN in toluene at selected times.
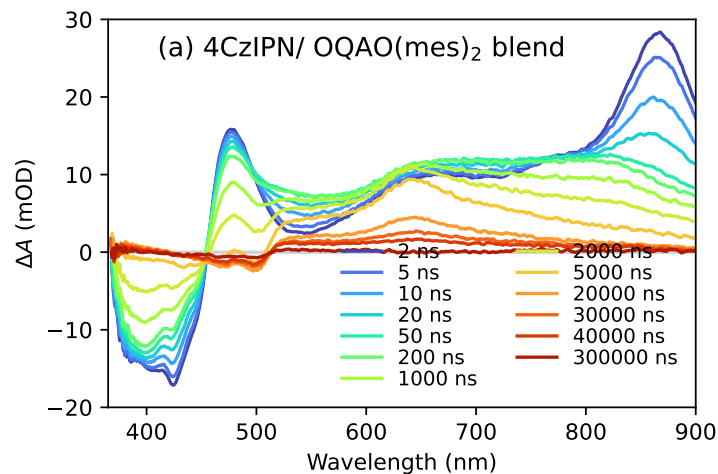
Figure S25: TA spectrum of 4CzIPN/OQAO(mes)$_2$ blend in toluene under N$_2$, excited at 355 nm.
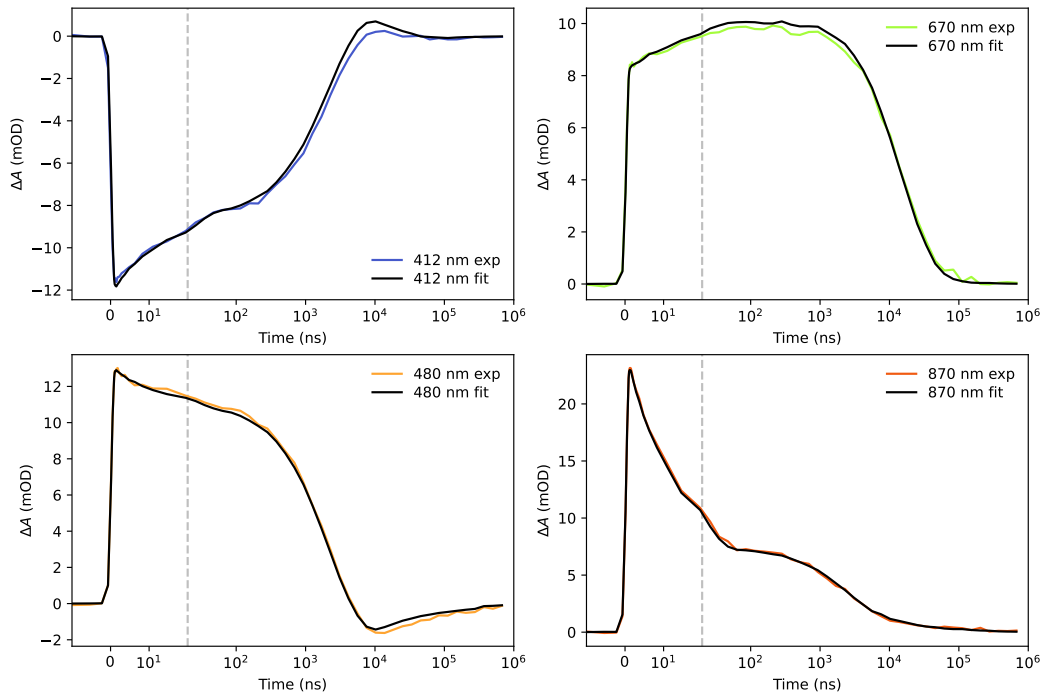
Figure S26: Fit of the neat 4CzIPN and OQAO(mes)$_2$ toluene basis spectra to the 4CzIPN/OQAO(mes)$_2$ blend TA at selected wavelengths. The vertical dashed line indicates a change from linear to log scale on the time axis.
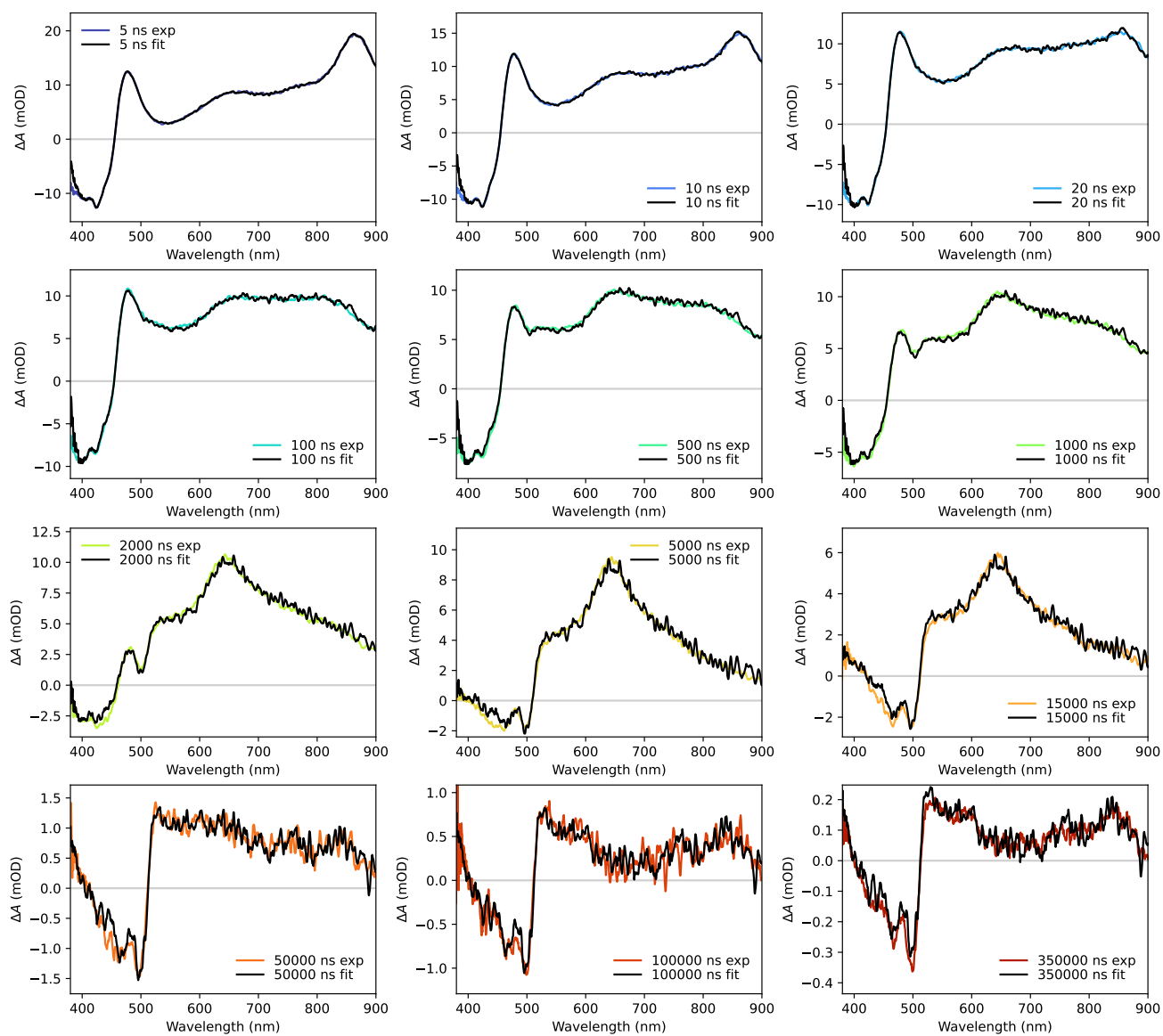
Figure S27: Fit of the neat 4CzIPN and OQAO(mes)₂ toluene basis spectra to the 4CzIPN/OQAO(mes)₂ blend TA at selected times.
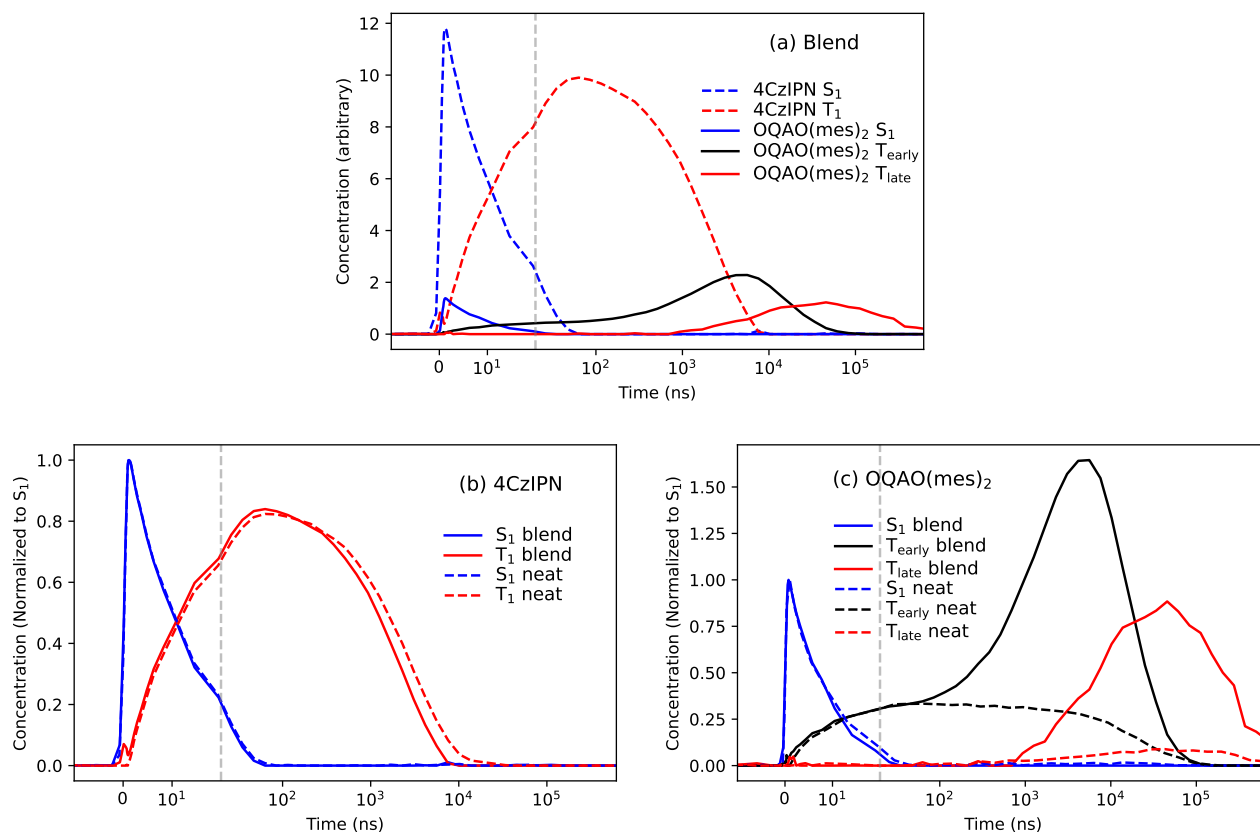
Figure S28: (a) Deconvoluted concentrations of excited states of 4CzIPN and OQAO(mes)$_2$ in the blend TA. (b) Comparison of the singlet and triplet kinetics of 4CzIPN in neat and blend TA. (c) Comparison of the singlet and triplet kinetics of OQAO(mes)$_2$ in neat toluene and blend TA. The 4CzIPN triplets decay faster in the blend than in the neat, and the OQAO(mes)$_2$ triplets are enhanced in the blend compared to the neat, indicating triplet energy transfer occurs from 4CzIPN to OQAO(mes)$_2$. This confirms that component B observed in the OQAO(mes)$_2$ spectrum is a triplet state, with energy below 2.53 eV.

S6   Excitation fluence dependence
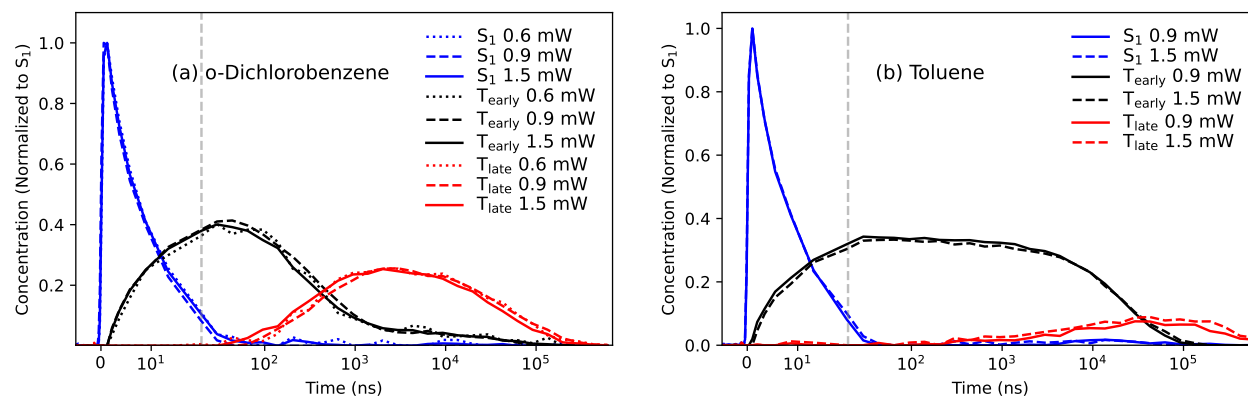
Figure S29: Fluence dependence of OQAO(mes)$_2$ in (a) o-dichlorobenzene and (b) toluene solutions, both at 298 K under N$_2$. No significant fluence dependence is observed, indicating that minimal bimolecular process, such as triplet-triplet annihilation, are negligible. Given emission data was recorded at substantially lower fluences than TA, we can also conclude that no bimolecular processes would be occurring in the emission data. The vertical dashed line indicates change from linear to logarithmic scale. Concentrations are determined using the upper limit of the component B (T$_{early}$) basis spectrum (i.e. assuming no T$_{late}$ is present at 55 ns).

S7   Effect of oxygen
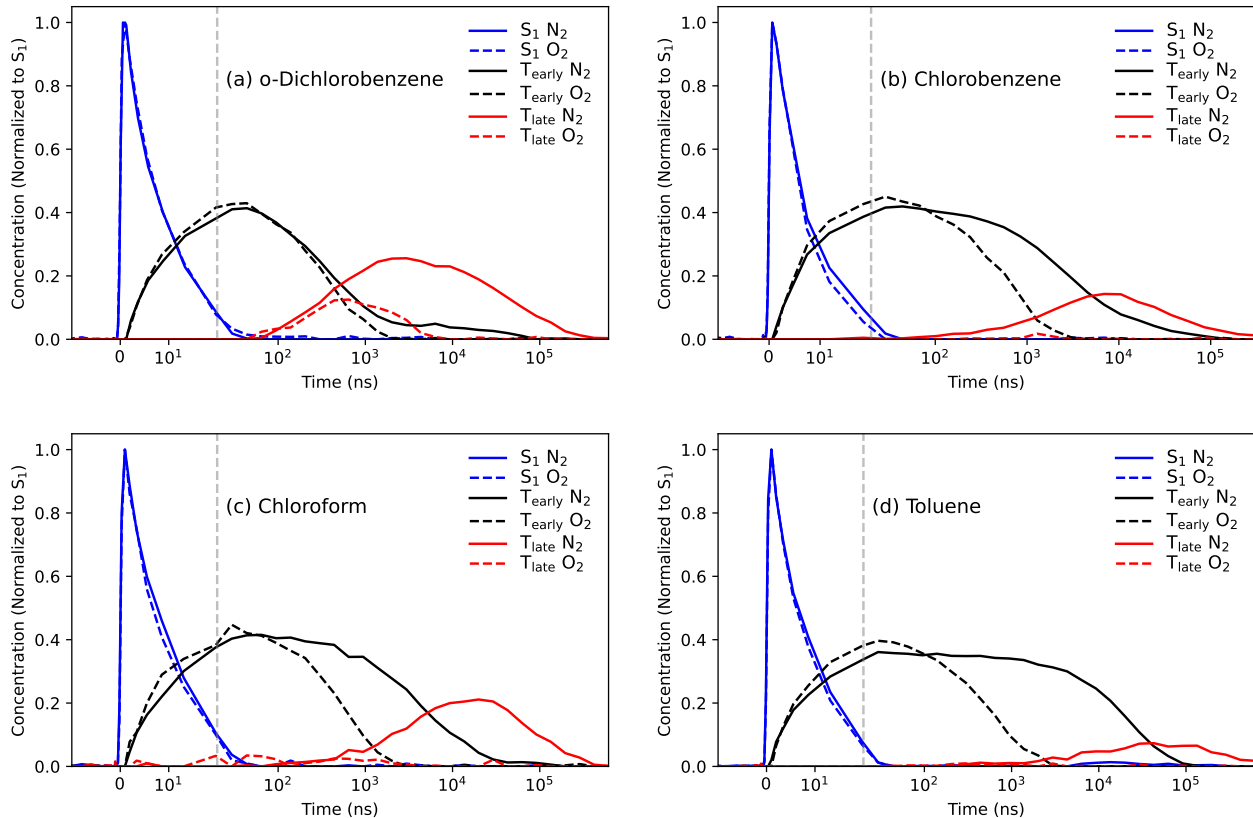
Figure S30: Oxygen dependence of OQAO(mes)$_2$ in various solvents at 298 K. The vertical dashed line indicates change from linear to logarithmic scale. Concentrations are determined using the upper limit of the component B (T$_{early}$) basis spectrum (i.e. assuming no T$_{late}$ is present at 55 ns). The triplet lifetimes are significantly shorter on exposure to oxygen, which agrees with the trends in delayed emission data in Figure S2.

S8   Kinetic modeling

TADF rates and efficiencies are often determined by fitting time-resolved emission data using equations derived from a two-state system (S$_1$ and T$_1$) and the quantum efficiencies of prompt and delayed emission.[7] However, since we measure prompt and delayed efficiency in separate measurements (TCSPC and MCS) we cannot determine relative quantum efficiencies of prompt and delayed emission. Additionally, there are clearly three states (S$_1$, T$_{early}$, and T$_{late}$) in our system. Therefore, rather than the typical equations used for time-resolved emission, we instead fit a full system of differential equations to our TA data, which allows us to take into account all three states, and in particular determine the dynamics between T$_{early}$, and T$_{late}$.

The deconvoluted concentrations from TA were fit to the TADF model in Figure S31. This model is equivalent to the system of differential equations

$$\frac{d[S_1]}{dt} = -k_{S_1}[S_1] - k_{ISC}[S_1] + k_{RISC}[T_{early}], \tag{S7a}$$

$$\frac{d[T_{early}]}{dt} = k_{ISC}[S_1] - k_{RISC}[T_{early}] - k_2[T_{early}] + k_{R2}[T_{late}] - k_{T_{early}}[T_{early}], \tag{S7b}$$

$$\frac{d[T_{late}]}{dt} = k_2[T_{early}] - k_{R2}[T_{late}] - k_{T_{late}}[T_{late}], \tag{S7c}$$
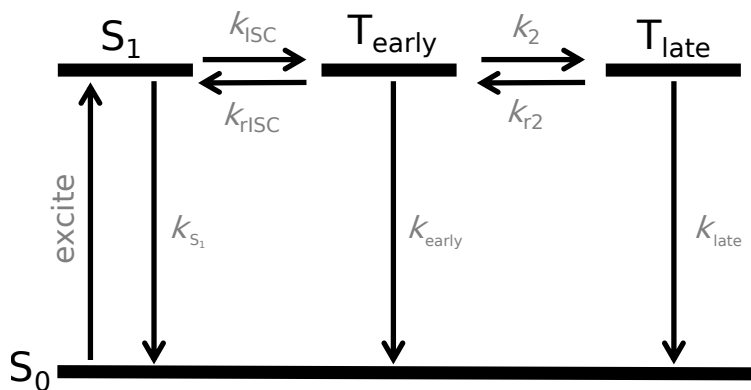
Figure S31: Model describing TADF. Note that energy levels are not necessarily to scale.

where $[S_1]$, $[T_{early}]$, and $[T_{late}]$ are the time dependent concentrations of the S_1, T_{early} and T_{late} excited states, and k_{S_1}, $k_{T_{early}}$, $k_{T_{late}}$ are their respective natural decay rates (radiative plus internal conversion). k_{ISC} and k_{RISC} are the forward and reverse rates of ISC, and k_2 and k_{R2} are the forward and reverse rates of conversion of T_{early} to T_{late} (i.e. internal conversion between triplet states).

Attempting to fit this model to the TA data of OQAO(mes)$_2$ under N_2 alone would result in rate constants with large uncertainties. In particular, the delayed fluorescence tail in the S_1 population is so small that is is not resolvable in the TA data, so there is not enough information to sensitively fit k_{RISC}. Additionally, since the absolute magnitudes of S_1, T_{early}, and T_{late} are unknown, the model was fit to normalized concentrations (i.e. the residuals were calculated between the fit and experimental concentrations normalized to their maximum value). This allows us to avoid the assumption that the basis spectra of each component are equal at the GSB (which is unlikely due to overlapping ESA and SE signals), but decreases the sensitivity of the fit. Thus, to counteract this and improve the sensitivity of the fit we also consider the photoluminescence quantum yields (PLQY), and the TA data under oxygen.

Since the delayed emission tail is absent under oxygen (Figure 1d), we assume that there is negligible contribution of triplet states to the PLQY under oxygen, i.e.

$$\text{PLQY}_{O_2} = \frac{k_r}{k_{prompt,O_2}} \tag{S8}$$

$$= \frac{k_r}{k_r + k_{nr} + k_{ISC} + k_{O_2,S_1}}, \tag{S9}$$

where k_{prompt,O_2} is the total prompt singlet decay under oxygen, k_r and k_{nr} are radiative and nonradiative decay rates of S_1 (i.e. $k_{S_1} = k_r + k_{nr}$), and k_{O_2,S_1} is the additional singlet quenching due to oxygen. Singlet quenching by oxygen is often neglected in TADF studies, but has been previously observed in other organic semiconductors.[2] Additionally, the difference in the S_1 lifetimes in TA (Figure S30) and the prompt emission decay (Figure 1c) under N_2 and O_2 suggests a small amount of oxygen quenching of singlet states is occurring here. k_{O_2,S_1} can be determined by comparing the prompt lifetimes of the deconvoluted S_1 concentrations in TA under N_2 and O_2:

$$k_{O_2,S_1} = k_{prompt,O_2} - k_{prompt,N_2}.$$

k_r can be determined from Equation S8:

$$k_r = \text{PLQY}_{O_2} \times k_{prompt,O_2}.$$

Finally, k_{ISC} can be calculated from:

$$k_{\text{ISC}} = k_{\text{prompt,O}_2} - k_{\text{r}} - k_{\text{nr}} - k_{\text{O}_2,\text{S}_1}.$$

If we take the nonradiative decay from the singlet state to be negligible, then an upper bound of k_{ISC} can be calculated. The actual k_{ISC} may be lower than this, but since the same approximation is made across all samples this has little effect on the conclusions drawn from this modeling. Additionally, the upper bounds of k_{ISC} calculated here give triplet yields of approximately 40%, which is roughly consistent with TA data. PLQYs under oxygen were determined in an integrating sphere, as reported in Table S1. These are averaged over 4 samples. The fraction of PLQYs under O_2 and N_2 ($\text{PLQY}_{\text{O}_2}/\text{PLQY}_{\text{N}_2}$) we also determined, using the fraction of integrated fluorescence intensities of samples prepared under O_2 and N_2, averaging over 8 samples for each solvent. The PLQY under N_2 was then determined from this fraction and the O_2 PLQY, as reported in Table S1. There are large uncertainties in the PLQYs, likely arising from varying oxygen contents between samples in different solvents, and in repeat experiments of the same solvent. There is also no apparent trend with solvent, so we conclude that the PLQYs both under N_2 and O_2 are the same within error. The prompt S_1 decay rates were determined by fitting a single exponential convoluted with the instrument response function to the deconvoluted S_1 concentrations from TA. $k_{\text{O}_2,\text{S}_1}$, k_{r}, and k_{ISC} were thus calculated from these prompt decays and PLQYs, with their corresponding time constants reported in Table S1.

Table S1: **Photoluminescence quantum yields (PLQY), the prompt S_1 decay lifetimes ($\tau_{\text{prompt,N}_2}$ and $\tau_{\text{prompt,O}_2}$), and calculated radiative (τ_{r}), intersystem crossing (τ_{ISC}), and oxygen quenching lifetimes ($\tau_{\text{O}_2,\text{S}_1}$). Note that the lifetimes are determined from fitting the S_1 component in the TA data, not from TCSPC.**

	PLQY_{O_2} [a]	$\frac{\text{PLQY}_{\text{O}_2}}{\text{PLQY}_{\text{N}_2}}$ [b]	PLQY_{N_2} [c]	$\tau_{\text{prompt,N}_2}$ [d]	$\tau_{\text{prompt,O}_2}$ [d]	τ_{ISC} [e]	τ_{r}	$\tau_{\text{O}_2,\text{S}_1}$
				(ns)	(ns)	(ns)	(ns)	(ns)
Toluene	0.56±0.08	0.89±0.01	0.63	7.7 ± 0.3	7.4 ± 0.3	18.5	13.3	191
Chloroform	0.64±0.04	0.88±0.01	0.73	9.3 ± 0.2	8.8 ± 0.3	28.9	13.8	163
Chlorobenzene	0.57±0.02	0.79±0.03	0.72	8.4 ± 0.2	6.6 ± 0.2	30.3	11.6	31
o-Dichlorobenzene	0.61±0.07	0.90±0.02	0.68	7.6 ± 0.3	7.6 ± 0.3	19.5	12.5	0
Total average	0.59±0.04	0.86±0.02	0.69					

[a] Errors are from an average over 4 experiments.
[b] Errors are from an average over 8 experiments.
[c] PLQY N_2 was calculated from PLQY_{O_2} and the O_2/N_2 PLQY fraction.
[d] Errors are 1.64× the standard deviation of the fit (i.e. a 90% confidence interval).
[e] Lower bound on τ_{ISC}, assuming $\tau_{\text{nr}} = \infty$

With k_{r} and k_{ISC} determined, the Model in Figure S31 and Equations S7a–c were fit to the data to find k_{RISC}, k_2, k_{R2}, $k_{\text{T}_{\text{early}}}$, and $k_{\text{T}_{\text{late}}}$. The sensitivity of k_{RISC} is still low, so we simultaneously fit both the data under N_2 and under O_2. The data under O_2 can be described by the same model, but with added oxygen quenching terms for each excited state:

$$\frac{\text{d}[\text{S}_1]}{\text{d}t} = -k_{\text{S}_1}[\text{S}_1] - k_{\text{ISC}}[\text{S}_1] + k_{\text{RISC}}[\text{T}_{\text{early}}] - k_{\text{O}_2,\text{S}_1}, \tag{S10a}$$

$$\frac{\text{d}[\text{T}_{\text{early}}]}{\text{d}t} = k_{\text{ISC}}[\text{S}_1] - k_{\text{RISC}}[\text{T}_{\text{early}}] - k_2[\text{T}_{\text{early}}] + k_{\text{R2}}[\text{T}_{\text{late}}] - k_{\text{T}_{\text{early}}}[\text{T}_{\text{early}}] - k_{\text{O}_2,\text{T}_{\text{early}}}, \tag{S10b}$$

$$\frac{\text{d}[\text{T}_{\text{late}}]}{\text{d}t} = k_2[\text{T}_{\text{early}}] - k_{\text{R2}}[\text{T}_{\text{late}}] - k_{\text{T}_{\text{late}}}[\text{T}_{\text{late}}] - k_{\text{O}_2,\text{T}_{\text{late}}}. \tag{S10c}$$

$k_{\text{O}_2,\text{S}_1}$ is calculated as explained above, and $k_{\text{O}_2,\text{T}_{\text{early}}}$ and $k_{\text{O}_2,\text{T}_{\text{late}}}$ are additionally fit to the data. In-

cluding the O_2 data allows us to additionally fit the ratios of PLQY under O_2 and N_2, which indicate the degree of RISC (after S_1 quenching is taken into account)x. Hence, in addition to fitting the excited state kinetics, the ratio of PLQY under O_2 and N_2 was also fit to the ratio of the integral of the modeled S_1 concentrations over the $9\,\mu s$ time window:

$$\frac{\text{PLQY}_{O_2}}{\text{PLQY}_{N_2}} = \frac{\int_{0\mu s}^{9\mu s} S_{1,O_2}(t)\mathrm{d}t}{\int_{0\mu s}^{9\mu s} S_{1,N_2}(t)\mathrm{d}t} \tag{S11}$$

Including this relation in the residuals of the fit significantly improves the sensitivity of k_{RISC}. The resulting fits for each solvent are shown in Figure S32, and the fitted time constants are given in Table S2. The proportions of excitons that undergo each process are also given in Table S3, where each proportion was calculated using the corresponding rate constants:

$$p_{\text{ISC}} = \frac{k_{\text{ISC}}}{k_{\text{ISC}} + k_{\text{r}}}, \tag{S12}$$

$$p_{\text{r}} = \frac{k_{\text{r}}}{k_{\text{ISC}} + k_{\text{r}}}, \tag{S13}$$

$$p_2 = \frac{k_2}{k_2 + k_{\text{RISC}} + k_{\text{T}_{\text{early}}}}, \tag{S14}$$

$$p_{\text{RISC}} = \frac{k_{\text{RISC}}}{k_2 + k_{\text{RISC}} + k_{\text{T}_{\text{early}}}}, \tag{S15}$$

$$p_{\text{T}_{\text{early}}} = \frac{k_{\text{T}_{\text{early}}}}{k_2 + k_{\text{RISC}} + k_{\text{T}_{\text{early}}}}, \tag{S16}$$

$$p_{\text{R2}} = \frac{k_{\text{R2}}}{k_{\text{R2}} + k_{\text{T}_{\text{late}}}}, \tag{S17}$$

$$p_{\text{T}_{\text{late}}} = \frac{k_{\text{T}_{\text{late}}}}{k_{\text{R2}} + k_{\text{T}_{\text{late}}}}. \tag{S18}$$

Table S2: Time constants resulting from the fit of Equations S7 and S10 to the deconvoluted TA data under N_2 and O_2 (using upper bound basis spectra). Errors are reported as $1.64\times$ the standard deviation of the fit (i.e. a 90% confidence interval). All time constants are reported in microseconds.

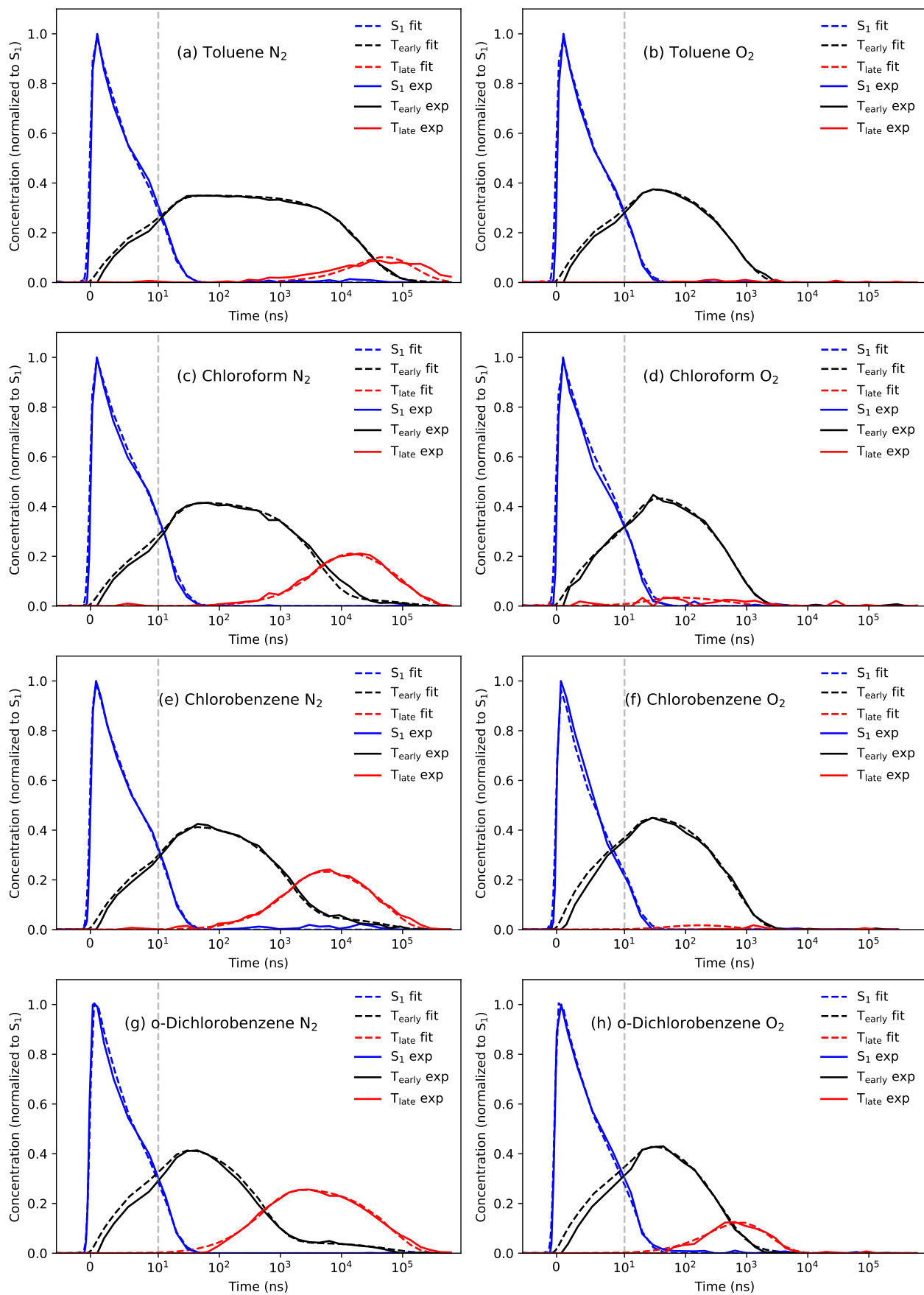|	τ_{RISC}	τ_2	τ_{R2}	$\tau_{\text{T}_{\text{early}}}$	$\tau_{\text{T}_{\text{late}}}$	$\tau_{\text{O2,T}_{\text{early}}}$	$\tau_{\text{O2,T}_{\text{late}}}$	$k_{\text{ISC}}/k_{\text{RISC}}$	k_2/k_{R2}
Toluene	156±16	55±3	240±30	52±3	210±30	0.66±0.03	1±3	4.4±0.7	8400±800
Chloroform	53±7	5.2±0.1	51±3	58±3	140±5	0.68±0.03	0.018±0.01	10.0±0.7	1800±200
Chlorobenzene	78±40	1.70±0.1	10.6±0.8	22±15	76±20	1.02±0.07	0.07±0.03	6.2±0.7	2600±1000
o-Dichlorobenzene	20±3	0.59±0.01	5.2±0.8	12±2	180±70	1.3±0.2	2.1±0.5	9±1	1000±200

Figure S32: Fits of the model in Figure S31 for each solvent. Left shows the fits to the TA data under N_2, and right the TA data under O_2.

Table S3: Proportions of excitons that undergo each process according to the time constants in Table S2. The destination state of each process is indicated in brackets.

	S$_1$		T$_{early}$			T$_{late}$	
	p_{ISC} (T$_{early}$)^a	p_r (S$_0$)^b	p_2 (T$_{late}$)^c	p_{RISC} (S$_1$)	$p_{T_{early}}$ (S$_0$)^d	p_{R2} (T$_{early}$)^e	$p_{T_{late}}$ (S$_0$)^d
Toluene	0.42	0.58	0.41	0.15	0.43	0.46	0.54
Chloroform	0.32	0.68	0.84	0.08	0.08	0.73	0.27
Chlorobenzene	0.28	0.72	0.91	0.02	0.07	0.88	0.12
o-Dichlorobenzene	0.39	0.61	0.93	0.03	0.05	0.97	0.03

^{a} Upper bound assuming no nonradiative decay.
^{b} Radiative decay to the ground state.
^{c} T$_{early}$ →T$_{late}$
^{d} Radiative plus nonradiative decay to the ground state.
^{e} T$_{late}$ →T$_{early}$

S8.1   Electrical excitation

With the fitted rate constants known, we can use the model described by Equations S7 to predict the different performances of OQAO(mes)$_2$ in a system with electrical injection (as in an OLED), rather than optical excitation. In other words, evaluating the model beginning from triplet states, rather than singlet. Since the recombination of charges yields 75% triplet excitons, and 25% singlet, we evaluated the model with initial singlet concentrations of 0.25, and triplet concentrations of 0.75. We consider two scenarios: either the T$_{early}$ state (i.e T$_2$) is directly generated from the recombination of charges (i.e [S$_1$(0),T$_{early}$(0),T$_{late}$(0)]=[0.25,0.75,0]), or the T$_{late}$ state is directly generated from the recombination of charges (i.e [S$_1$(0),T$_{early}$(0),T$_{late}$(0)]=[0.25,0,0.75]). The model is evaluated using both the toluene parameters and *o*-dichlorobenzene parameters (Table S2). To determine the efficiency of light generation in an OLED scenario, we add an additional population to the model to describe the photons emitted from the S$_1$ state:

$$\frac{d[S_1]}{dt} = -k_{S_1}[S_1] - k_{ISC}[S_1] + k_{RISC}[T_{early}], \tag{S19a}$$

$$\frac{d[T_{early}]}{dt} = k_{ISC}[S_1] - k_{RISC}[T_{early}] - k_2[T_{early}] + k_{R2}[T_{late}] - k_{T_{early}}[T_{early}], \tag{S19b}$$

$$\frac{d[T_{late}]}{dt} = k_2[T_{early}] - k_{R2}[T_{late}] - k_{T_{late}}[T_{late}], \tag{S19c}$$

$$\frac{d[photons]}{dt} = k_{S_1}[S_1], \tag{S19d}$$

where k_{S_1} is the rate of radiative decay from S$_1$. The total number of photons generated is the maximum of the [photons] population. The efficiency can be described as

$$\text{efficiency} = \frac{\text{photons out}}{\text{excitons in}} \tag{S20}$$

$$= \frac{\text{max[photons]}}{S_1(0) + T_{early/late}(0)} \tag{S21}$$

To determine to contribution of the triplet states, we also evaluated the model with the initial singlet concentration equal to zero (i.e [S$_1$(0),T$_{early}$(0),T$_{late}$(0)]=[0,0,0.75]). The resulting evaluated models are shown in Figures S33–S35, and the efficiencies are reported for different initial populations in Table S4.

The efficiencies predicted by this model (when injecting 25% singlet and 75% triplet) are comparable to the external quantum efficiencies reported for OQAO devices by Zou et al. (20.3%), though real devices will have several additional loss pathways not considered by this model, particularly from the outcoupling

of light. The photophysics in the solid state is also likely to differ from solution.[8] Only a small proportion of the emitted photons are from TADF: for toluene less than 35% of emitted light comes from TADF, and for o-dichlorobenzene approximately 45% is from TADF. When injecting T_{late} states rather than T_{early}, the efficiency drops. For o-dichlorobenzene, this is only by 2%, since the reverse reaction of T_{late} to T_{early} is relatively efficient. For toluene, however, the efficiency drops by 54% when exciting T_{late} rather than T_{early}.

The efficiency is higher for o-dichlorobenzene, but this is predominantly because of the differences in ISC and radiative singlet decay rates, which in term comes from PLQYs, for which there is a large degree of error. If we fix these rate constants (k_{ISC}, k_{rISC}, and k_{S_1}) to be the same as in toluene, we see the efficiency is much lower than toluene.

Finally, we also compared the performance when injecting T_{early} with the conversion to T_{late} turned off, i.e. $k_2 = 0$ (Figure S35). For both toluene and o-dichlorobenzene, the efficiency increases by approximately 43%. This further demonstrates that, although some conversion of T_{late} back to T_{early} occurs, it ultimately acts as a loss pathway.

Table S4: Efficiency of S_1 emission (photons out/ excitons in) simulated using the model described by Equations S19 at different initial conditions, using the parameters fit to the TA data for toluene and o-dichlorobenzene (Table S2).

$[S_1(0),T_{early}(0),T_{late}]$	[0.25,0.75,0]	[0.25,0,0.75]	[0,0.75,0]	[0,0,0.75]	[0,0.75,0]*
Max photons toluene	0.243	0.197	0.086	0.039	0.123
Max photons o-dichlorobenzene	0.314	0.310	0.143	0.139	0.204
Max photons o-dichlorobenzene[†]	0.169	0.169	0.021	0.020	0.032

*evaluated with $k_2 = 0$

[†] evaluated with toluene parameters for k_{ISC}, k_{rISC}, and k_{S_1}.
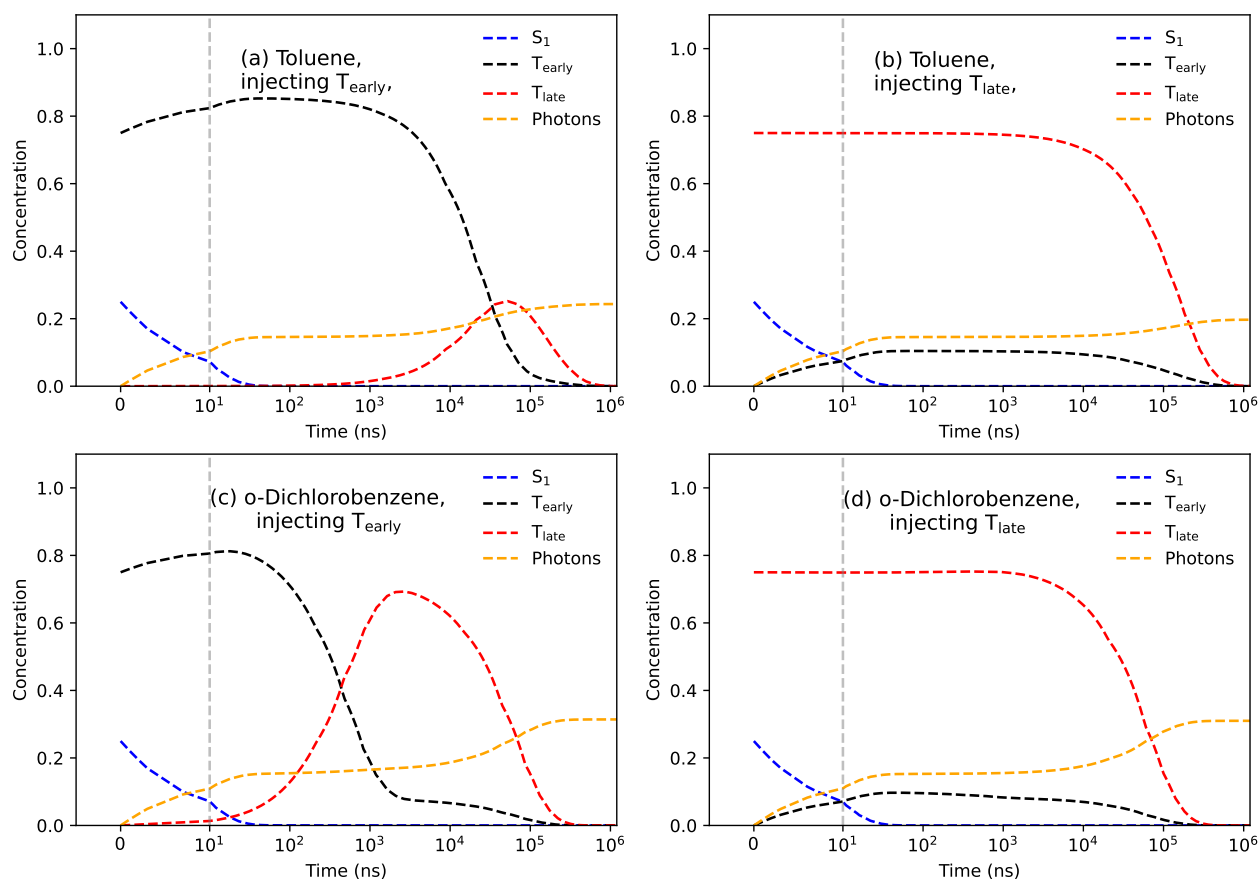
Figure S33: Model evaluated using initial concentrations of $[S_1(0),T_{early}(0),T_{late}]=[0.25,0.75,0]$) (a and c), and $[S_1(0),T_{early}(0),T_{late}]=[0.25,0,0.75]$) (b and d), for toluene (a and b) and *o*-dichlorobenzene (c and d).

Figure S34: Model evaluated using initial concentrations of $[S_1(0),T_{early}(0),T_{late}]=[0,0.75,0]$ (a and c), and $[S_1(0),T_{early}(0),T_{late}]=[0,0,0.75]$ (b and d), for toluene (a and b) and *o*-dichlorobenzene (c and d).
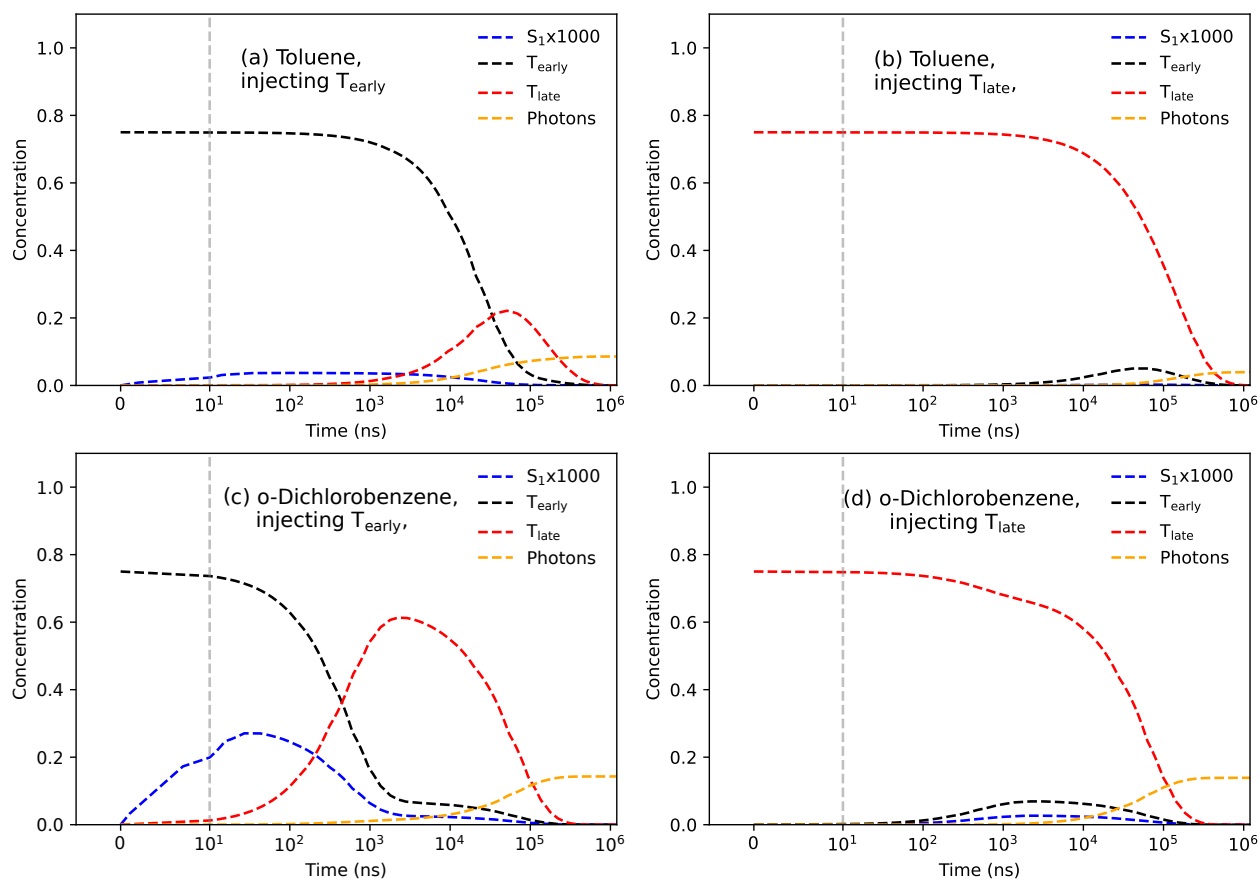

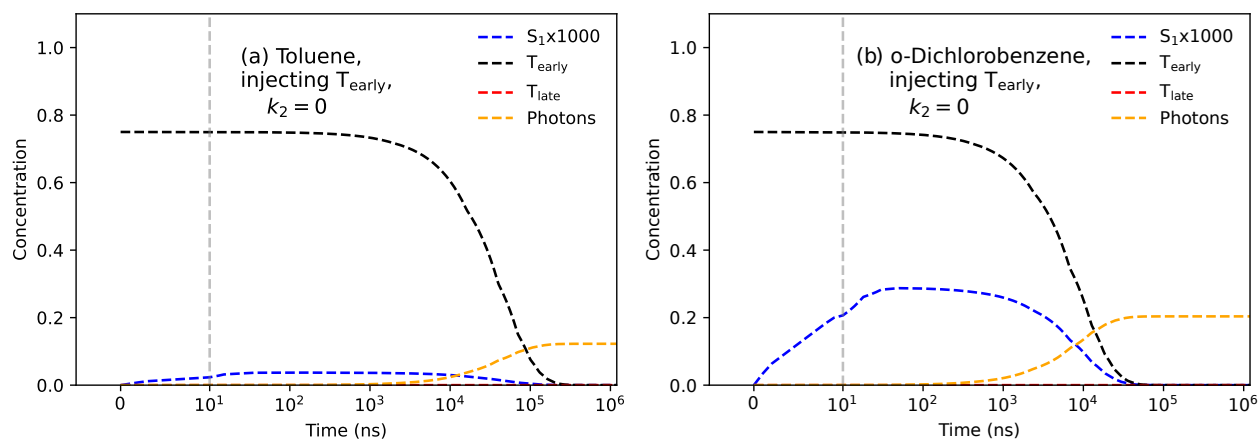**Figure S35:** Model evaluated using initial concentrations of $[S_1(0),T_{early}(0),T_{late}]=[0,0.75,0]$ with no T_{late} formation, i.e. $k_2=0$, for toluene (a) and *o*-dichlorobenzene (b).

S8.2   Sensitization modeling

We also briefly fit a kinetic model to the deconvoluted triplet sensitization data, to determine whether T_{late} is also sensitized by 4CzIPN. The system of differential equations used was:

$$\frac{d[S_1]}{dt} = -k_{S_1}[S_1] - k_{ISC}[S_1] + k_{RISC}[T_{early}], \tag{S22a}$$

$$\frac{d[T_{early}]}{dt} = k_{ISC}[S_1] - k_{RISC}[T_{early}] - k_2[T_{early}] + k_{R2}[T_{late}] - k_{T_{early}}[T_{early}]$$
$$+ k_{TET_1}[\text{4CzIPN } T_1], \tag{S22b}$$

$$\frac{d[T_{late}]}{dt} = k_2[T_{early}] - k_{R2}[T_{late}] - k_{T_{late}}[T_{late}] + k_{TET_2}[\text{4CzIPN } T_1], \tag{S22c}$$

$$\frac{d[\text{4CzIPN } S_1]}{dt} = -k_{ISC,4CzIPN}[\text{4CzIPN } S_1] + k_{RISC,4CzIPN}[\text{4CzIPN } T_1], \tag{S22d}$$

$$\frac{d[\text{4CzIPN } T_1]}{dt} = k_{ISC,4CzIPN}[\text{4CzIPN } S_1] - k_{RISC,4CzIPN}[\text{4CzIPN } T_1] - k_{TET_1}[\text{4CzIPN } T_1]$$
$$- k_{TET_2}[\text{4CzIPN } T_1], \tag{S22e}$$

where all parameters are as described above, with the addition of $k_{ISC,4CzIPN}$ and $k_{RISC,4CzIPN}$ as the forward and reverse rates of ISC in 4CzIPN, and k_{TET_1} and k_{TET_2} as the rate constants of triplet energy transfer from 4CzIPN to the OQAO(mes)$_2$ T_{early} and T_{late} states, respectively. For simplicity, we neglected the radiative and internal conversion decays of 4CzIPN, and only focus on the rates of triplet energy transfer. The rate of triplet energy transfer to the T_{early} state was fit as much larger than that to the T_{late} state, ($\tau_{TET_1} = 2390 \pm 160$, $\tau_{TET_2} = 13000 \pm 3000$), with the fit shown in Figure S36a. This corresponds to just 15% of 4CzIPN triplets transferring to the T_{late} state. Additionally, the data can feasibly be fit with k_{TET_2} constrained to zero (Figure S36b), indicating that triplet energy transfer may exclusively occur to the T_{early} (T_2) state.

It is unclear why there would be a selectivity for energy transfer to the T_{early} state. Since T_{late} is presumably lower in energy, there would be more of an energetic driving force for transfer to the T_{late} state. It is possible that the electronic coupling between 4CzIPN and OQAO(mes)$_2$ triplets may therefore be the dominant factor in the energy transfer rate, and since the molecular orbital arrangements between the T_{early} and T_{late} states are different, it is not unreasonable that the coupling of the 4CzIPN triplet to these states would be different.
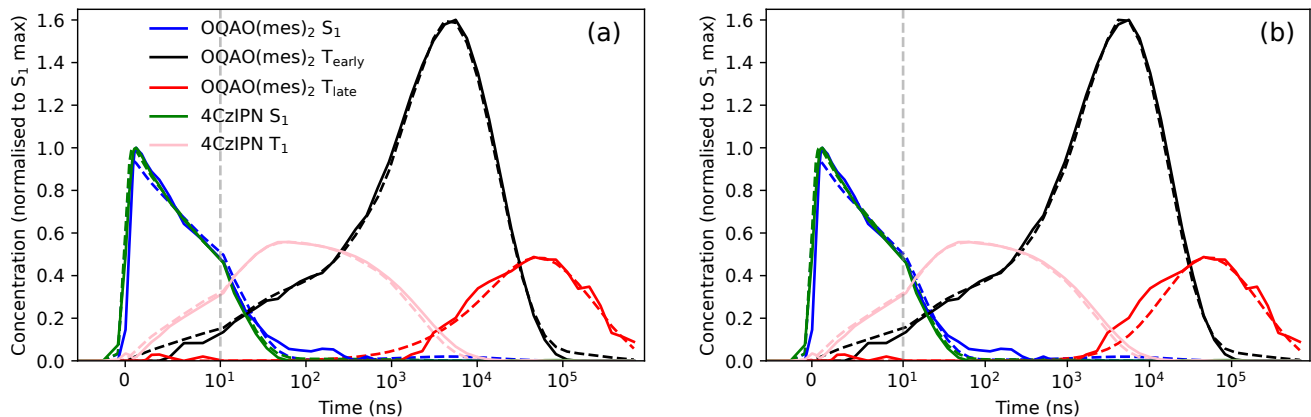

Figure S36: Fit of a kinetic model to the deconvoluted concentrations of the blend 4CzIPN and OQAO(mes)$_2$ system. (a) Includes triplet energy transfer from 4CzIPN to both OQAO(mes)$_2$ triplet states. (b) Only includes triplet energy transfer to the OQAO(mes)$_2$ T_{early} state ($k_{TET_2} = 0$).

S8.3   Lower bound basis spectrum modeling

We additionally attempted to fit a kinetic model to the concentrations determined from deconvolution with the lower bound of the T_{early} (component B) basis spectrum. These kinetics better resemble a concurrent rise of T_{early} and T_{late} ($A \longrightarrow B + C \longrightarrow C$), hence we modified the kinetic model used to describe the upper bound data (Equations S7) to include a direct S_1 to T_{late} pathway with rate constant k_{ISC2}:

$$\frac{d[S_1]}{dt} = -k_{S_1}[S_1] - k_{ISC}[S_1] + k_{RISC}[T_{early}] - k_{ISC2}[S_1], \tag{S23a}$$

$$\frac{d[T_{early}]}{dt} = k_{ISC}[S_1] - k_{RISC}[T_{early}] - k_2[T_{early}] + k_{R2}[T_{late}] - k_{T_{early}}[T_{early}], \tag{S23b}$$

$$\frac{d[T_{late}]}{dt} = k_{ISC2}[S_1] + k_2[T_{early}] - k_{R2}[T_{late}] - k_{T_{late}}[T_{late}], \tag{S23c}$$

where all other parameters are as described previously. Figure S37 shows the fits of this model to the o-dichlorobenzene data. The model overestimates the T_{early} component at late times, and is unable to capture the dynamics between the two triplet populations as well as the Fits in Figure S32.
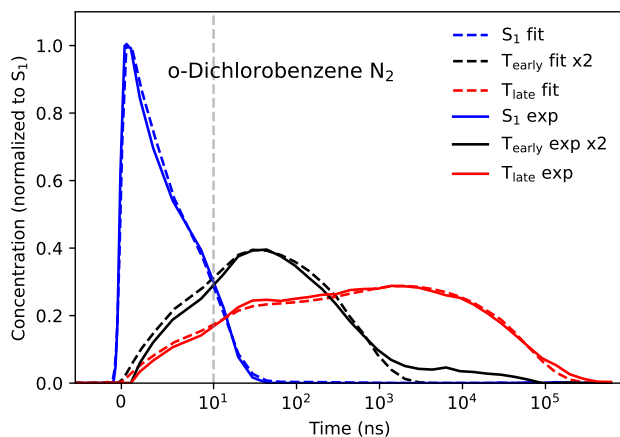
Figure S37: Fits of the model in Equations S23 to the o-dichlorobenzene data deconvoluted with the lower bound basis spectrum for T_{early} (component B).

S9   Computational details

Using the Gaussian 16 Rev. B.01 package,[9] structures were optimized using density functional theory (DFT) at the OT-S-LC-ωhPBE/6-31G(d)/IEFPCM(toluene) level of theory to determine the ground state geometries. The α, β, and ω parameters for the OT-S-LC-ωhPBE functional were non-empirically tuned for each molecule as previously described.[10] Frequency analysis was performed at the same level of theory to verify the absence of imaginary frequencies.

Since many common DFT functionals are known to inaccurately predict the photophysical properties of MR-TADF emitters,[11] multiple functionals including OT-S-LC-ωhPBE, SOS-PBE-QIDH, MPW1KCIS, and TPSSh were benchmarked to the experimental absorbance spectrum of OQAO(mes)$_2$ using the time-dependent DFT (TDDFT) under the Tamm-Dancoff approximation with the 6-31G(d) basis set and the IEFPCM(toluene) solvation model. This revealed that TDDFT calculations at the TDA-TPSSh/6-31G(d)/IEFPCM(toluene) level of theory most accurately predict the properties of OQAO(mes)$_2$ (Figure S38).

The first 25 singlet and triplet vertical excitations at the ground state geometry were analyzed using the
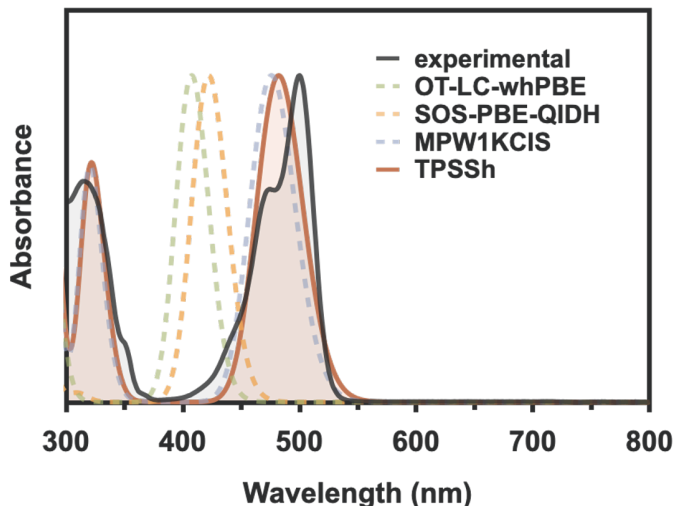
Figure S38: Normalized experimental and computed absorption spectra for OQAO(mes)$_2$. Experimental spectra were measured in toluene and computed spectra were calculated using TDA-TDDFT with the functional indicated, the 6-31G(d) basis set, and the IEFPCM(toluene) solvation model.

TDA-TDDFT at the TPSSh/6-31G(d)/IEFPCM(toluene) level of theory. Hole-electron analysis[12] and calculation of the lambda index[13] were performed using formatted checkpoint files from these TDDFT calculations along with the Multiwfn 3.8 program.[14] VESTA 3.5.7 was used to simultaneously visualize both the electron and hole isosurfaces, with an isovalue of 0.001.[15] TDA-TDDFT was performed using ORCA 5.0.3 at the TPSSh/6-31G(d)/CPCM(toluene) level of theory to compute the spin orbit coupling constants between the singlet and triplet states at the ground state geometry.[16,17] Spin-orbit coupling constants computed at other levels of theory are shown in Table S6.

Table S5:   Parameters determined from TDA-TDDFT calculations at the TPSSh/6-31G(d)/IEFPCM(toluene) level of theory for OQAO(mes)$_2$. Λ indicates the extent of overlap between electron and hole. Energies reported are a qualitative indicator of the ordering of the states.

	Energy (eV)	Λ	oscillator strength for $S_0 \rightarrow S_n$
S_1	2.57	0.61	0.2646
S_2	3.14	0.24	0.0000
T_1	2.09	0.61	-
T_2	2.88	0.41	-

Table S6: Spin-orbit coupling (SOC) constants for OQAO(mes)$_2$ calculated using multiple functionals and basis sets in combination with the CPCM(toluene) solvation model.

Functional	TPSSh/ 6-31G(d)	TPSSh/ def2-SVP	OT-S-LC-whPBE/ 6-31G(d)	B3LYP/ 6-31G(d)
T_1–S_1 SOC (cm^{-1})	0.00	0.00	0.00	0.00
T_2–S_1 SOC (cm^{-1})	0.02	0.02	0.02	0.02

Table S7: Coordinates for the optimized ground state geometry of OQAO(mes)$_2$.

Atom	X (Å)	Y (Å)	Z (Å)	Atom	X (Å)	Y (Å)	Z (Å)
C	0.00000000	1.19902500	-0.90640100	C	0.00000000	7.20587100	2.90735900
C	0.00000000	1.17072800	0.49351400	H	-2.13789800	7.06255100	2.80495100
C	0.00000000	2.34209300	1.22162600	H	2.13789800	7.06255100	2.80495100
C	0.00000000	3.59122800	0.58412500	C	0.00000000	-4.84425300	1.38998600
C	0.00000000	3.62130100	-0.79981600	C	-1.21655700	-5.43270200	1.76621600
C	0.00000000	2.43993600	-1.54896400	C	1.21655700	-5.43270200	1.76621600
H	0.00000000	2.27245100	2.30390300	C	-1.19428300	-6.60517400	2.51804200
H	0.00000000	4.55964900	-1.34254200	C	1.19428300	-6.60517400	2.51804200
N	0.00000000	0.00000000	-1.62283800	C	0.00000000	-7.20587100	2.90735900
C	0.00000000	1.21706600	-3.70998600	H	-2.13789800	-7.06255100	2.80495100
C	0.00000000	1.19462300	-5.10307600	H	2.13789800	-7.06255100	2.80495100
C	0.00000000	0.00000000	-2.99754600	C	-2.52927300	4.82068500	1.36309200
C	0.00000000	0.00000000	-5.80689300	H	-2.62914600	4.76656900	0.27445700
H	0.00000000	2.15297900	-5.61046800	H	-2.62932400	3.79753600	1.73931900
C	0.00000000	-1.21706600	-3.70998600	H	-3.36695200	5.40503300	1.75000500
C	0.00000000	-1.19462300	-5.10307600	C	2.52927300	4.82068500	1.36309200
H	0.00000000	0.00000000	-6.89055200	H	2.62932400	3.79753600	1.73931900
H	0.00000000	-2.15297900	-5.61046800	H	2.62914600	4.76656900	0.27445700
C	0.00000000	-1.17072800	0.49351400	H	3.36695200	5.40503300	1.75000500
C	0.00000000	-2.34209300	1.22162600	C	0.00000000	8.45330200	3.74443100
C	0.00000000	-1.19902500	-0.90640100	H	0.00000000	8.20994400	4.81289800
C	0.00000000	-3.59122800	0.58412500	H	0.88513600	9.06459300	3.55049800
H	0.00000000	-2.27245100	2.30390300	H	-0.88513600	9.06459300	3.55049800
C	0.00000000	-2.43993600	-1.54896400	C	2.52927300	-4.82068500	1.36309200
C	0.00000000	-3.62130100	-0.79981600	H	2.62914600	-4.76656900	0.27445700
H	0.00000000	-4.55964900	-1.34254200	H	2.62932400	-3.79753600	1.73931900
C	0.00000000	2.51185400	-3.01761700	H	3.36695200	-5.40503300	1.75000500
C	0.00000000	-2.51185400	-3.01761700	C	-2.52927300	-4.82068500	1.36309200
O	0.00000000	-3.57803100	-3.61775000	H	-2.62932400	-3.79753600	1.73931900
O	0.00000000	3.57803100	-3.61775000	H	-2.62914600	-4.76656900	0.27445700
O	0.00000000	0.00000000	1.19475100	H	-3.36695200	-5.40503300	1.75000500
C	0.00000000	4.84425300	1.38998600	C	0.00000000	-8.45330200	3.74443100
C	-1.21655700	5.43270200	1.76621600	H	0.88513600	-9.06459300	3.55049800
C	1.21655700	5.43270200	1.76621600	H	0.00000000	-8.20994400	4.81289800
C	-1.19428300	6.60517400	2.51804200	H	-0.88513600	-9.06459300	3.55049800
C	1.19428300	6.60517400	2.51804200				

S10   Solid state photophysics

We finally turn to the photophysics of $OQAO(mes)_2$ in the solid state, suspended in thin film matrices of either poly(methyl methacrylate) (PMMA, dielectric constant of ~2), or poly(vinylidene fluoride-co-hexafluoropropylene) (PVDF-HFP, dielectric constant of 8.4). The steady-state emission and absorption are shown in Figure S39. Our intention was to study the solid-state photophysics in two different dielectric environments, however, even with the bulky mesityl groups, $OQAO(mes)_2$ is very susceptible to aggregation.[1] As a result the steady-state absorbance is significantly red-shifted from solution, and changes little between PMMA and PVDF-HFP, indicating the environment is likely dominated by surrounding aggregated chromophores. This also results in a substantial amount of excimer formation, evident from the broad-red shifted emission shoulder with a longer prompt emission lifetime, characteristic of excimer formation. PVDF-HFP shows more excimer formation than PMMA, potentially owing to its lower glass transition temperature, which allows molecules to rearrange and aggregate. The delayed fluorescence of PVDF-HFP also a more biexponential decay, suggesting the presence of bimolecular processes in this system, which could also result from more extensive aggregation. The excimer formation and bimolecular annihilation complicate the photophysics in the solid state, so we do not attempt to analyze the photophysics in detail. We primarily comment on the shape of the TA spectra in Figure S39c and d. The TA in both polymer matrices show significantly less spectral evolution than in solution. There is some change over very early times, corresponding from S_1 conversion to triplet excitons, but after the first few nanoseconds the shape is relatively constant. The resolution is much lower than for solution, so there could be some very small evolution at late times that is unresolvable at this level of noise, but it would regardless be significantly less than in solution. The prompt emission spectra and early time component of the TA spectra decay much faster than in solution, potentially due to increased amounts of nonradiative decay. Intriguingly, the late time spectra differ between PMMA and PVDF-HFP, with the former baring a closer resemblance to the T_{early} state (T_2), and the latter the T_{late} state (T_1). Additionally, we see that the delayed emission lifetime corresponds well to the decay of the TA. We could speculate that in PMMA, the low polarity prevents any formation of the late time T_{late} state, thus the spectrum resembles the T_{early} states in solution, whereas in PVDF-HFP, the high polarity bring the T_{early} and T_{late} states into equilibrium. However it is just as likely that differing aggregation in the two matrices can lead to different spectral shapes. To further resolve the excited-state dynamics additional experiments are needed, such as higher resolution TA, or time-resolved electron paramagnetic resonance, which could be interesting avenues of future study. It should be noted that other factors may alter the photophysical properties in solution as well, such as exciplex formation with host-matrices in OLEDs, which has previously been shown to increase TADF efficiency.[18]
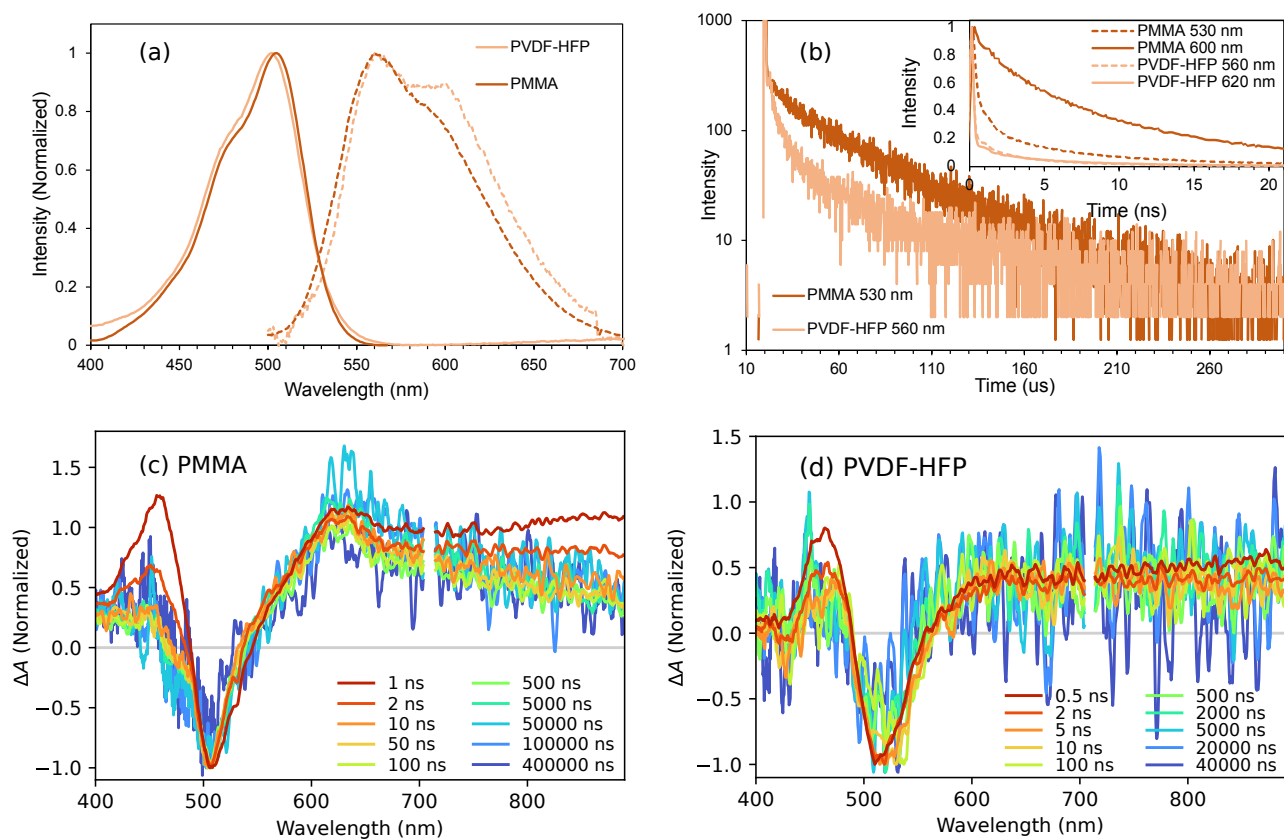
Figure S39: (a) Steady-state absorption (full lines) and emission (dashed lines) of OQAO(mes)$_2$ in solid matrices of PMMA and PVDF-HFP. (b) Prompt (inset) and delayed emission of OQAO(mes)$_2$ in solid matrices in PMMA and PVDF-HFP at 298 K under vacuum. (c) TA spectra of OQAO(mes)$_2$ in a PMMA matrix and (d) in a PVDF-HFP matrix, both at 298 K under vacuum, normalized to the GSB.

S11   Additional code and data

Raw transient absorption data, time-resolved emission data, and code for the deconvolution and modelling of transient absorption data can be found at `https://hdl.handle.net/2123/32599`

S12   References

(1) Cho, I.; Kendrick, W. J.; Stuart, A. N.; Ramkissoon, P.; Ghiggino, K. P.; Wong, W. W. H.; Lakhwani, G. Multi-resonance TADF in optical cavities: suppressing excimer emission through efficient energy transfer to the lower polariton states. *J. Mater. Chem. C* **2023**, *11*, 14448–14455.

(2) Stuart, A. N.; Kee, T. W.; Huang, D. M. Role of Singlet and Triplet Excited States in the Oxygen-Mediated Photophysics and Photodegradation of Polyacenes. *J. Am. Chem. Soc.* **2024**, *146*, 2174–2186.

(3) Forecast, R.; Campaioli, F.; Schmidt, T. W.; Cole, J. H. Photochemical Upconversion in Solution: The Role of Oxygen and Magnetic Field Response. *J. Phys. Chem. A* **2023**, *127*, 1794–1800.

(4) Huang, S.; Zhang, Q.; Shiota, Y.; Nakagawa, T.; Kuwabara, K.; Yoshizawa, K.; Adachi, C. Computational Prediction for Singlet- and Triplet-Transition Energies of Charge-Transfer Compounds. *J. Chem. Theory Comput.* **2013**, *9*, 3872–3877.

(5) Lu, J.; Pattengale, B.; Liu, Q.; Yang, S.; Shi, W.; Li, S.; Huang, J.; Zhang, J. Donor-Acceptor Fluorophores for Energy-Transfer-Mediated Photocatalysis. *J. Am. Chem. Soc.* **2018**, *140*, 13719–13725.

(6) Hosokai, T.; Matsuzaki, H.; Nakanotani, H.; Tokumaru, K.; Tsutsui, T.; Furube, A.; Nasu, K.; Nomura, H.; Yahiro, M.; Adachi, C. Evidence and mechanism of efficient thermally activated delayed fluorescence promoted by delocalized excited states. *Sci. Adv.* **2017**, *3*, e1603282.

(7) Tsuchiya, Y.; Diesing, S.; Bencheikh, F.; Wada, Y.; dos Santos, P. L.; Kaji, H.; Zysman-Colman, E.; Samuel, I. D. W.; Adachi, C. Exact Solution of Kinetic Analysis for Thermally Activated Delayed Fluorescence Materials. *J. Phys. Chem. A* **2021**, *125*, 8074–8089.

(8) Zou, S.-N.; Peng, C.-C.; Yang, S.-Y.; Qu, Y.-K.; Yu, Y.-J.; Chen, X.; Jiang, Z.-Q.; Liao, L.-S. Fully Bridged Triphenylamine Derivatives as Color-Tunable Thermally Activated Delayed Fluorescence Emitters. *Org. Lett.* **2021**, *23*, 958–962.

(9) Frisch, M. J.; Trucks, G. W.; Schlegel, H. B.; Scuseria, G. E.; Robb, M. A.; Cheeseman, J. R.; Scalmani, G.; Barone, V.; Petersson, G. A.; Nakatsuji, H. et al. Gaussian 16 Revision B.01. 2016; Gaussian Inc. Wallingford CT.

(10) Bergmann, K.; Hojo, R.; Hudson, Z. M. Uncovering the Mechanism of Thermally Activated Delayed Fluorescence in Coplanar Emitters Using Potential Energy Surface Analysis. *J. Phys. Chem. Lett.* **2023**, *14*, 310–317.

(11) Madayanad Suresh, S.; Hall, D.; Beljonne, D.; Olivier, Y.; Zysman-Colman, E. Multiresonant Thermally Activated Delayed Fluorescence Emitters Based on Heteroatom-Doped Nanographenes: Recent Advances and Prospects for Organic Light-Emitting Diodes. *Adv. Funct. Mater.* **2020**, *30*, 1908677.

(12) Liu, Z.; Lu, T.; Chen, Q. An sp-hybridized all-carboatomic ring, cyclo[18]carbon: Electronic structure, electronic spectrum, and optical nonlinearity. *Carbon* **2020**, *165*, 461–467.

(13) Peach, M. J. G.; Benfield, P.; Helgaker, T.; Tozer, D. J. Excitation energies in density functional theory: An evaluation and a diagnostic test. *J. Chem. Phys.* **2008**, *128*, 044118.

(14) Lu, T.; Chen, F. Multiwfn: A multifunctional wavefunction analyzer. *J. Comput. Chem.* **2012**, *33*, 580–592.

(15) Momma, K.; Izumi, F. *VESTA3* for three-dimensional visualization of crystal, volumetric and morphology data. *J. Appl. Crystallogr.* **2011**, *44*, 1272–1276.

(16) Neese, F. The ORCA program system. *WIREs Comput. Mol. Sci.* **2012**, *2*, 73–78.

(17) Neese, F. Software update: The ORCA program system—Version 5.0. *WIREs Comput. Mol. Sci.* **2022**, *12*, e1606.

(18) Wu, X.; Su, B.-K.; Chen, D.-G.; Liu, D.; Wu, C.-C.; Huang, Z.-X.; Lin, T.-C.; Wu, C.-H.; Zhu, M.; Li, E. Y. et al. The role of host-guest interactions in organic emitters employing MR-TADF. *Nat. Photonics* **2021**, *15*, 780–786.